

JANUARY 2015

M.Sc. in Engineering Physics

ALİ TUNÇ

**UNIVERSITY OF GAZİANTEP
GRADUATE SCHOOL OF
NATURAL & APPLIED SCIENCES**

**INVESTIGATION OF THE CHARACTERISTICS OF THE
BORON DOPED MnO FILMS DEPOSITED BY SPRAY
PYROLYSIS METHOD**

**M. Sc. THESIS
IN
ENGINEERING PHYSICS**

**BY
ALİ TUNÇ
JANUARY 2015**

**Investigation of the Characteristics of the Boron Doped MnO Films
Deposited by Spray Pyrolysis Method**

M.Sc. Thesis

in

Engineering Physics

University of Gaziantep

Supervisor

Prof. Dr. Metin BEDİR

by

Ali TUNÇ

January 2015

©2015 [ALİ TUNÇ].

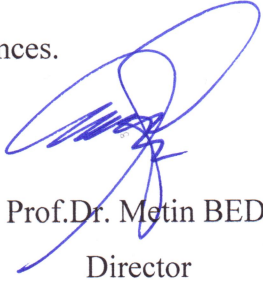
REPUBLIC OF TURKEY
UNIVERSITY OF GAZİANTEP
GRADUATE SCHOOL OF NATURAL & APPLIED SCIENCES
ENGINEERING PHYSICS

Name of the thesis: Investigation of the characteristics of the boron doped MnO films deposited by spray pyrolysis method.

Name of the student: Ali TUNÇ

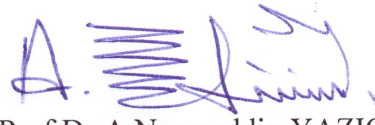
Exam date:29.01.2015

Approval of the Graduate School of Natural and Applied Sciences.



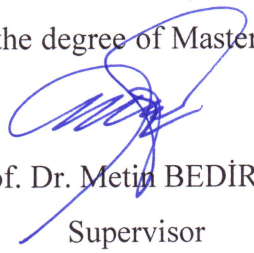
Prof.Dr. Metin BEDİR
Director

I certify that this thesis satisfies all the requirements as a thesis for the degree of Master of Science/Doctor of Philosophy.



Prof.Dr.A.Necmeddin YAZICI
Head of Department

This is to certify that we have read this thesis and that in our consensus/majority opinion it is fully adequate, in scope and quality, as a thesis for the degree of Master of Science/Doctor of Philosophy.



Prof. Dr. Metin BEDİR
Supervisor

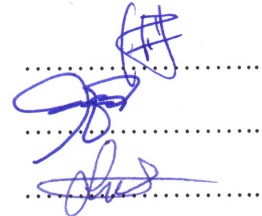
Examining Committee Members

Prof.Dr.Mustafa ÖZTAŞ

Prof.Dr. Metin BEDİR

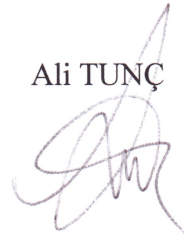
Assist.Prof.Dr.Serap SUR ÇELİK

Signature



I hereby declare that all information in this document has been obtained and presented in accordance with academic rules and ethical conduct. I also declare that, as required by these rules and conduct, I have fully cited and referenced all material and results that are not original to this work.

Ali TUNÇ

A handwritten signature in black ink, appearing to be 'Ali TUNÇ', written in a cursive style.

ABSTRACT

INVESTIGATION OF THE CHARACTERISTICS OF THE BORON DOPED MNO FILMS DEPOSITED BY SPRAY PYROLYSIS METHOD

TUNÇ, ALİ

M.Sc. in Engineering Physics

Supervisor: Prof. Dr. Metin BEDİR

January 2015

60 pages

In this study, the influence of boric acid concentration on the structural and optical properties of sprayed MnO:B films were widely investigated by using different techniques. Boron-doping was achieved by adding 0.1M, 0.2M, 0.3M and 0.4M H₃BO₃ to the starting solution. The crystal structure of the undoped and boron doped films were determined from x-ray diffraction peaks. The diffraction pattern exhibit peaks at $2\theta=28.4098^\circ$, $2\theta=47.2858^\circ$ and $2\theta=56.0638^\circ$ were identified to be (111), (220) and (311) planes having cubic structure with lattice parameter, approximetly, $a=5.4\text{\AA}$. The band gap of the films were changed from 2.25 to 2.54 eV with boron concentration. The slight decreases in the optical band gap of the films with the increasing boron concentration. The surface morphology of the sprayed undoped and boron doped films were analysed by scanning electron microscopy (SEM).

Key words: Spray pyrolysis method, MnO:B film, Structural and optical properties.

ÖZ

Püskürtme Metodu ile Elde Edilen Bor Katkılı MnO Filmlerin Karakterizasyonunun Araştırılması

TUNÇ, ALİ

Yüksek Lisans Tezi, Fizik Müh. Bölümü

Tez Yöneticisi: Prof. Dr. Metin BEDİR

Ocak 2015

60 sayfa

Bu çalışmada, püskürtme yöntemiyle elde edilen MnO filmlerin yapısal ve optik özellikleri üzerinde borik asit konsantrasyonunun etkisi çeşitli teknikler kullanılarak incelenmiştir. Bor katkılanması, 0.1 M, 0.2 M, 0.3 M ve 0.4 M H₃BO₃ 'ün başlangıç çözeltisine ilave edilmesiyle başarılmıştır. Bor katkısız ve bor katkılı filmlerin kristal yapısı X-ışını kırılma yöntemiyle tespit edilmiştir. Kırılma deseninden elde edilen maksimum pik değerleri $2\theta=28,4098^\circ$, $2\theta=47,28580^\circ$ ve $2\theta=56,0638^\circ$ karşılık gelen (111), (220) ve (311) yüzeylerinde ve yaklaşık kafes parametresi, $a=5.4\text{Å}$ kübik yapıya sahip olduğu belirlenmiştir. Optiksel ölçümlerden filmlerin yasak enerji bandı aralığının bor konsantrasyonu ile 2,25eV'den 2.54 eV'a değiştiği ve bu değişimin bor konsantrasyonu artışı ile azaldığı tespit edilmiştir. Bor katkısız ve bor katkılı filmlerin yüzey morfolojisi taramalı elektron mikroskobu (SEM) ile analiz edilmiştir.

Anahtar Kelimeler: Püskürtme yöntemi, MnO:B film, yapısal ve optiksel özellikler.

ACKNOWLEDGEMENTS

The author wishes to express his deepest gratitude to his supervisor Prof. Dr. Metin BEDİR for his guidance, advice, criticism, encouragements and insight throughout the research.

The author and supervisor would like to thank to Prof. Dr. Ahmet Kaya for his help to take XRD patterns of the films.

The author and supervisor would like to thank to Prof. Dr. Mustafa ÖZTAŞ for reviewing our study and making positive recommendation.

The author and supervisor would like to thank to Engineering Physics Department of Gaziantep University for giving opportunity to do this study and the experiments.

The author would also like to thank to his mother and his wife for great support and encouragements.

TABLE OF CONTENTS

ACKNOWLEDGMENT.....	VII
TABLE OF CONTENTS.....	VIII
LIST OF TABLES.....	X
LIST OF FIGURES.....	XI
LIST OF SYMBOLS/ABBREVIATIONS.....	XII
CHAPTER 1.....	1
INTRODUCTION.....	1
CHAPTER 2.....	4
CRYSTAL STRUCTURE.....	4
2.1 Unit Cell.....	4
2.1.2 Miller Indices.....	5
2.1.3 Hexagonal Structure.....	6
2.2 Semiconductor Materials.....	8
2.2.1 Intrinsic Semiconductors.....	12
2.2.2 Extrinsic Semiconductors.....	12
2.2.3 Semiconductor Doping.....	13
2.2.4 N-Type Doping.....	14
2.2.5 P-Type Doping.....	15
2.3 Optical Transition.....	16
2.3.1 Optical Absorption.....	18
2.4 X-Ray Diffraction Method.....	20
2.5 Scanning Electron Microscope Measurement.....	23
CHAPTER 3.....	26
EXPERIMENTAL STUDIES.....	26
3.1 Spray Pyrolysis Method.....	26
3.1.1 Experimental Set up.....	27
3.1.2 Substrate Preparation.....	27
3.1.3 Solution Preparation.....	28
3.1.4 Development of MnO Films.....	28
3.1.5 Development of Boron Doped MnO Films.....	29

CHAPTER 4.....	30
RESULTS AND DISCUSSION.....	30
4. XRD Analysis of MnO and Boron Doped MnO Films.....	30
4.1 Introduction.....	30
4.2 Crystal Structure.....	30
4.3 Lattice Constant (a) Studies.....	33
4.4 Grain Size Studies.....	34
4.5 Microstrain Studies.....	37
4.6 Dislocation Density Studies.....	41
4.7 Optical Studies.....	43
4.8 SEM Studies.....	46
4.9 Elemental Analysis.....	50
5. Conclusion	52
REFERENCES.....	53

LIST OF TABLES

TABLES	Page
Table 2.1. Resistivity and Conductivity at 20°C	9
Table 2.2. Semiconductor donors and acceptors	14
Table 4.1. XRD pattern results of the undoped and boron doped MnO films	40
Table 4.2. The band gap values of the samples with respect to the Molar ratio of the manganese chloride and boric acid.....	45
Table 4.3. The variation of Mn and O composition in MnO films.....	51

LIST OF FIGURES

LIST OF FIGURES	Page
Figure 2.1. Illustration of unit cell.....	4
Figure 2.2. Three dimensional figures of Bravais Lattices.....	5
Figure 2.3. Hexagonal structure coordinates.....	6
Figure 2.4. Diagrams for calculating the volume of HCP unit cell.....	7
Figure 2.5. Band gap illustrations of metal, semiconductor and insulator.....	10
Figure 2.6. The periodic table of the elements.....	11
Figure 2.7. Two-dimensional illustration of the crystal lattice of an n-type semiconductor.....	15
Figure 2.8. Two-dimensional illustration of the crystal lattice of and p-type semiconductor.....	16
Figure 2.9. Band gap illustration of direct transition and indirect transition.....	17
Figure 2.10 Three dimensional solid matter.....	19
Figure 2.11 Optical absorption in a semiconductor.....	19
Figure 2.12. Path difference of reflected ray and transmitted then reflected ray.....	21
Figure 2.13. Basic parts of SEM.....	24
Figure 3.1. Experimental set up of spray pyrolysis.....	27
Figure 3.2 Cleaning process of substrate.....	28
Figure 4.1. XRD patterns of undoped and boron doped MnO films with the different concentrations of boric acid in the starting solution.....	33
Figure 4.2. Variation of the grain size (d) with different boron concentration in MnO films.....	35
Figure 4.3. Variation of the microstrain (ϵ) with boron concentration in MnO films.....	38
Figure 4.4. Variation of the dislocation density (ρ) with boron concentration in MnO films.....	42

Figure 4.5. A representative graph showing the dependence of $(\alpha hv)^2$ (eV/cm) ² on the photon energy hv (eV).....	45
Figure 4.6. Variation of the optical gap E_{opt} with the boron concentration in solution.....	46
Figure 4.7 SEM images of the MnO and boron doped MnO films.....	47
Figure 4.8. EDS spectra of sprayed MnO film.....	50

LIST OF SYMBOLS/ABBREVIATIONS

MnO	Manganese Monooxide
MnO:B	Boron Doped Manganese Monooxide
HCP	Hexagonal Close-Packed
SEM	Scanning Electron Microscope
XRD	X-Ray Diffraction
EDS	Energy Dispersive X-Ray Analysis

CHAPTER 1

INTRODUCTION

The polycrystalline semiconductors have attracted much interest in an expanding variety of applications in various electronic and optoelectronic devices. The technological interest in polycrystalline based devices is mainly caused by their very low production costs. Considerable attention has been paid to doped semiconductors as they offer multifunctional properties beyond those of ideal semiconductors [1]. In general, the characteristics of the films and related applications have been dominated by several factors, such as grain boundary, grain size, crystallinity, resistivity and optical and magnetic permeability, which are interrelated with utilized deposition and treatment methods and their variables [2–4]. In particular, materials known as diluted magnetic semiconductors (DMS) which have an interesting combination of magnetism and semiconductivity, have attracted widespread scientific attention due to their prospective applications in magneto-optical and spintronic devices. In DMS, the band electrons and holes strongly interact with the localized magnetic moments and cause a variety of interesting phenomena [2,3]. MnO and boron doped MnO films can be prepared by different techniques such as radio-frequency sputtering[5], solvo-thermal synthesis[6], hydro-thermal method [7], molecular beam epitaxy [8], thermal vacuum evaporation [9], successive ionic layer adsorption and reaction (SILAR) [10], chemical bath deposition (CBD) [11], and spray pyrolysis [12-13]. Manganese oxide (MnO) is a transitional material having interesting physical and chemical properties. It has opto-electronic applications and is often used in electrode materials [14, 15], electrochemical capacitors [16,17], rechargeable batteries, sensors [18], magnetoelectronic devices [19]. AFurther, MnO has been used as a substrate in the synthesis of magnetic oxide perovskite compounds, which have a variety of electrical and magnetic properties similar to metal insulator transistors [20-22]. MnO of different structures are deposited using several techniques such as sol-gel [19], thermal evaporation in vacuum [23], and

MOCVD [24]. The spray pyrolysis technique has been applied to deposit a wide variety of thin films [25]. MnO is paramagnetic at room temperature and has a crystal structure of the NaCl type ($a_0 \sim 4.44 \text{ \AA}$). At 118 K, MnO bulk crystals undergo a first order paramagnetic to antiferromagnetic phase transition [26, 27]. Due to the variable valence of manganese cations the chemistry of its compounds is very rich. This holds true for manganese oxides as well. There are several stable manganese oxides that also occur as minerals. MnO occurs in nature as a green-colored mineral manganosite and has a so-called rock salt structure that can be considered the insertion of two FCC lattices, which are composed up of Mn^{2+} and O^{2-} ions [28]. In natural environments, manganese occurs in the Mn(II), Mn(III) and Mn(IV) oxidation states. All three valences form a large number of oxide minerals, ranging from the simple phases manganosite (MnO), partridgeite (Mn_2O_3) and pyrolusite (MnO_2) to complex mixed-valence oxides such as birnessite $((\text{Ca,Na})(\text{Mn}^{2+}, \text{Mn}^{4+})_7 \text{O}_{14} \cdot 3\text{H}_2\text{O})$ and todorokite $((\text{Na,Ca,K,Ba,Mn}^{2+})_2\text{Mn}_5\text{O}_{12} \cdot 3\text{H}_2\text{O})$ [29]. Among the 3d transition metal oxides, manganese monoxide (MnO) is of particular importance due to the high spin ground state of the $3d^5$ configuration of Mn^{2+} . Therefore, MnO could be an excellent model system to investigate many kinds of spin dependent or magnetic interactions between of MnO in the bulk from has been extensively studied for many years. [30] During the literature review, we were unable to find any records about boron doped MnO films, but there are some records about usage of boron in other films, for example boron doped ZnO films. Boron doped ZnO films have the potential to an effective technique for improving the conversion efficiency of Cu(In,Ga)Se₂ (CIGS) thin film solar cells [31], especially silicon thin film solar cells [32]. However, there exist some uncertain factors that influence the physical properties of ZnO:B thin film. Because of the smaller ion radius of boron, it can act as either interstitial boron or substitute done in ZnO lattice [33]. Additionally, the effects of boron doping on the properties of CdS thin films have been investigated to determine the proper doping level for good quality films by Lee et al. [34]. The spray pyrolysis method used in this work is based on a chemical deposition technique where ionic solutions of the desired film materials are sprayed onto a preheated substrate. Films prepared by the spray pyrolysis technique are predominantly polycrystalline and their properties are significantly influenced by deposition procedures [35]. The spray pyrolysis method,

which was used in the 1940s, is an economic and easy way of producing films. Mochel produced SnO_2 films by using SnCl_2 in 1951. In 1960s Chamberlina and Skarman produced CdS films with this method. Ma, Fahrenburch and Bube produced CdS/CdTe solar cells with this method [36]. One of the most widely used doping atoms for fullerenes is boron, since it can form a stable structure with them. The structural and optical properties of boron doped fullerene $\text{C}_{60}(\text{B}:\text{C}_{60})$ thin films have been studied by several researchers. Theoretically, boron can improve the conductivity of carbon materials, since it lowers their Fermi energy level [37]. Boron-doped diamond (BDD) thin film is one of the new promising materials for electrochemical applications due to its unique and extremely useful properties [38]. Electro-analysis is one field that can benefit from the attractive electrochemical properties of diamond thin film as an electrode material [39]. These properties including a low and stable voltammetric background current, a wide working potential window in aqueous electrolyte solutions (2.5 – 3 V) [40], slight adsorption of polar organic molecules and good activity toward some redox analytes without any conventional pretreatment [41]. It has been demonstrated that nanocrystalline MnO thin film electrodes show high rate performance, low polarization and good cyclic performance. Results indicate that MnO is a promising high capacity anode material for lithium ion batteries [42].

According to our knowledge, no report exists in the literature on the synthesis of boron doped MnO films by spray pyrolysis technique. Therefore, we have turned our attention to the study of the feasibility of spray pyrolysis technique for the synthesis of MnO:B films. In this study, the influence of boric acid concentration on the structural and optical properties of sprayed MnO:B films are investigated.

CHAPTER 2

CRYSTAL STRUCTURE

2.1 Unit Cell

Solids are classified into two groups according to their structure. If the solid material atoms, molecules or ions are arranged in an ordered pattern it is called crystal. If the solid material atoms, molecules or ions are not arranged in an ordered pattern it is called amorphous.

Crystal structure has a repeating pattern and the smallest shape of that crystal is called as unit cell. Unit cells have the same symmetry throughout the crystal.

Unit cell is defined by three independent vectors, which are, \vec{a} , \vec{b} , and \vec{c} , and three angles which are between these vectors, α , β and γ .

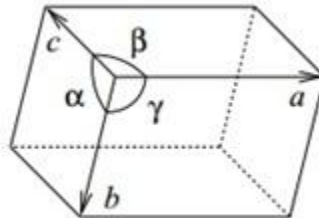


Figure 2.1 Illustration of a unit cell [43].

The volume of the unit cell is given by

$$V = abc\sqrt{1 - \cos^2 \alpha - \cos^2 \beta - \cos^2 \gamma + 2 \cos \alpha \cos \beta \cos \gamma} \quad (2.1)$$

According to these parameters unit cells are categorized into seven.

- ❖ Cubic: The lengths of all axes are equal and all angles between the axes are 90° . There are three types; simple cubic, body-centered cubic, and face-centered cubic.

- ❖ Tetragonal: The lengths of two axes are equal but the length of the third axis is different. All angles between the axes are 90° . There are two types, simple tetragonal and body-centered tetragonal.
- ❖ Orthorhombic: The lengths of all axes are different. All angles between the axes are 90° . There are four types: simple orthorhombic, body-centered orthorhombic, face-centered orthorhombic and end-centered orthorhombic.
- ❖ Hexagonal: The lengths of two axes are equal but the length of the third axis is different. Two of the angles between the axes are 90° , but the third angle is 120° .
- ❖ Rhombohedral (trigonal): The lengths of all axes are equal. All angles between the axes are equal but different than 90° .
- ❖ Monoclinic: The lengths of all axes are different. $\alpha = \gamma = 90^\circ$, $\beta \neq 90^\circ$. There are two types: simple monoclinic and end-centered monoclinic.
- ❖ Triclinic: The lengths of all axes are different. Angles: $\alpha \neq \beta \neq \gamma \neq 90^\circ$

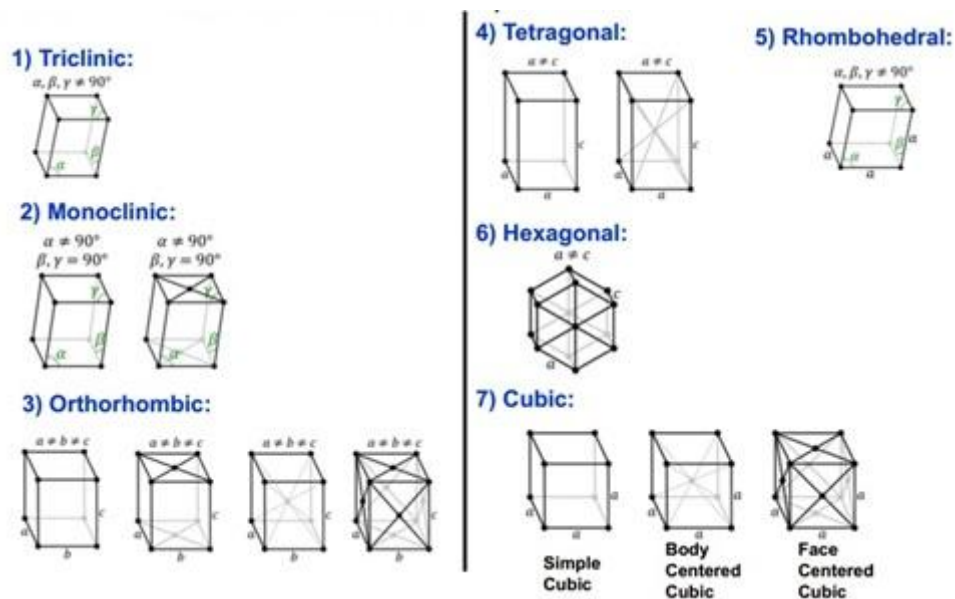


Figure 2.2 Three dimensional figures of Bravais Lattices [44].

2.1. 2 Miller Indices

In 1839, a British mineralogist William Hallowes Miller introduced a notation system for directions and planes in crystal lattice. Miller indices indicate planes and directions in crystal. There are three indices: h represents the perpendicular plane to x -axis, k represents the perpendicular plane to y -axis, and l represents the perpendicular plane to z -axis. With different symbols we introduce different

information; (hkl) representation is for a particular plane, whereas $\{hkl\}$ representation is for a family of planes. Similarly, $[hkl]$ representation is for a particular direction and $\langle hkl \rangle$ representation is for a family of directions. When commas are used (h,k,l) , this notation represents a point. In the Miller indices, there are no fractions. All numbers must be integer, and if there are fractions all indices must be multiplied by a number that changes fractions to integers. Negative numbers are shown with a bar above the number, for example -2 is shown as $\bar{2}$.

We can represent a vector which passes from origin to a lattice point;

$$\vec{r} = \vec{r}_1 a + \vec{r}_2 b + \vec{r}_3 c \quad (2.2)$$

where: $\vec{r}_1, \vec{r}_2, \vec{r}_3$ are miller indices and a,b,c are basic vectors.

Miller indices are used like;

2.1.3 Hexagonal Structure

Hexagonal structure is defined by four axes. Three of these axes are equal and they are interchangeable. Angles between the positive ends (or negative ends) of these three equal axes are 120° . These three axes lie in same horizontal plane. And the fourth axis is perpendicular to this horizontal plane.

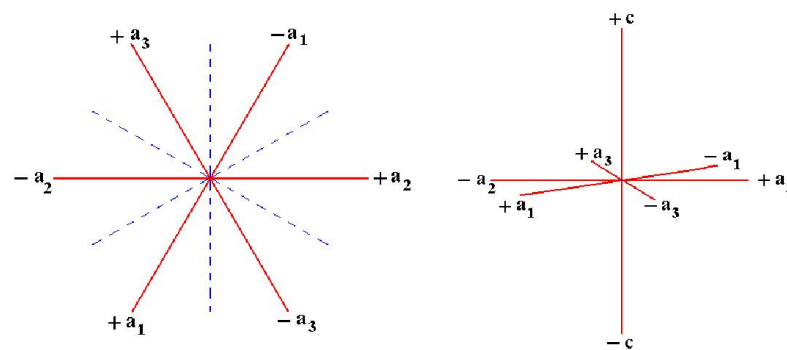


Figure 2.3 Hexagonal structure coordinates [45].

Hexagonal structure is different from other crystal structures because it has four axes, so for the Hexagonal structure the Bravais-Miller method is adopted. We have four indexes, h, k, i and l. In order to convert three indexes to four indexes we use following equations;

If we show three indexes as; h', k', l' and four indexes as; h, k, i, l

$$h=(2h'-k')/3 \quad (2.3)$$

$$k=(2k'-h')/3 \quad (2.4)$$

$$i=-(h+k) \quad (2.5)$$

$$l=l' \quad (2.6)$$

In a hexagonal close packed structure there are:

- 12 atoms at the corners shared by 6 cells,
- Two center atoms (one at the top, one at the bottom) shared by two cells,
- Three mid-plane unshared atoms

Thus, there are $(12 \times 1/6) + (2 \times 1/2) + (3) = 6$ atoms per unit cell. The ratio of lattice parameters c/a is 1.633.

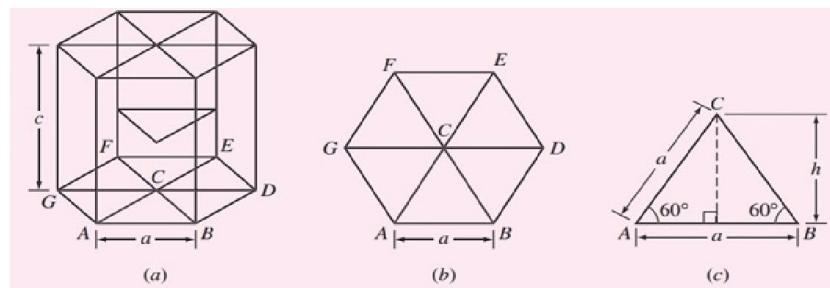


Figure 2.4 Diagrams for calculating the volume of an HCP unit cell. (a) HCP unit cell. (b) Base of HCP unit cell. (c) Triangle ABC removed from base of unit cell [46].

We can calculate the volume of a unit cell. The area of the triangle shown in the figure is equal to;

$$\frac{a \cdot a \sin 60}{2} = a \frac{2\sqrt{3}}{4} \quad (2.7)$$

We have 6 triangles on the base so;

$$V = (6 \times a \frac{2\sqrt{3}}{4}) \times c = \frac{3\sqrt{3}}{2} a^2 c \quad (2.8)$$

The atomic packing factor calculation of Hexagonal close-packed is

$$a=2r \quad (2.9)$$

$$c = \sqrt{\frac{2}{3}}(4r) \quad (2.10)$$

It is then possible to calculate the APF as follows:

$$\text{APF} = \frac{N_{\text{atoms}} \times V_{\text{atom}}}{V_{\text{crystal}}} = \frac{6x(4/3)\pi r^3}{[(3\sqrt{3}/2)(a^2)(c)]} \quad (2.11)$$

$$= \frac{6x(4/3)\pi r^3}{[(3\sqrt{3}/2)(2r^2)(\sqrt{2/3}4r)]} = \frac{\pi}{\sqrt{18}} \approx 0.74 \quad (2.12)$$

In cubic structures we can calculate the lattice spacing with the following formula

$$\frac{1}{d_{hkl}^2} = \frac{h^2 + k^2 + l^2}{a^2} \quad (2.13)$$

But for hexagonal structure we have to use the following Formula

$$\frac{1}{d_{hkl}^2} = \frac{4}{3} \frac{h^2 + hk + k^2}{a^2} + \frac{l^2}{c^2} \quad (2.14)$$

$a=2r$ and $c=\sqrt{2/3} 4r$ and so $a = \sqrt{6}c/4$

We know that Bragg's law is

$$n\lambda = 2d \sin\theta \quad (2.15)$$

We can then calculate the size of the crystal "D" and measure for the width of the microstrain distribution "e" with the following equations;

$$\beta_L = \frac{\lambda}{D \cos\theta} \quad (2.16)$$

$$\beta_G = 4\epsilon \tan\theta \quad (2.17)$$

where β_L is the integral breadth of the Lorentzian component and β_G is the integral breadth of the Gaussian component [47].

2.2 Semiconductor Materials

In earlier time people classified materials as either conductors or insulators. If a material allows electricity to pass through it, that material is called a conductor, if a material does not allow electricity to pass through it that is called an insulator. Later,

scientist researches showed us that there are some materials which are between conductors and insulators.

Conductors have one, two or three electrons in their last orbit, and when we apply a voltage difference these electrons start to move, resulting in an electric current. Insulators have six, seven or eight electrons in their last orbit and the bond between these electrons are strong. When a voltage difference is applied to insulators, their electrons do not start to move, and this prevents electricity from passing through insulators.

Each material has a resistivity to electricity. That depends on four parameters: type of material, length, cross sectional area and temperature.

The resistivity of conductors is very low, while that is in insulators is very high. Semiconductors have a resistivity value that is between those of conductors and insulators. A table of resistivity and conductivity for some materials is;

Table 2.1 Table of resistivity and conductivity at 20°C [48].

Material	ρ ($\Omega\cdot\text{m}$) at 20 °C Resistivity	σ (S/m) at 20 °C Conductivity
Silver	1.59×10^{-8}	6.30×10^7
Copper	1.68×10^{-8}	5.96×10^7
Aluminum	2.82×10^{-8}	3.5×10^7
Manganin	4.82×10^{-7}	2.07×10^6
Carbon (amorphous)	5×10^{-4} to 8×10^{-4}	1.25 to 2×10^3
Carbon (diamond)	1×10^{12}	$\sim 10^{-13}$
Germanium	4.6×10^{-1}	2.17
Sea water	2×10^{-1}	4.8
Drinking water	2×10^1 to 2×10^3	5×10^{-4} to 5×10^{-2}
Silicon	6.40×10^2	1.56×10^{-3}
Deionized water	1.8×10^5	5.5×10^{-6}
Glass	10×10^{10} to 10×10^{14}	10^{-11} to 10^{-15}
Air	1.3×10^{16} to 3.3×10^{16}	3×10^{-15} to 8×10^{-15}

The main reason that different materials have different resistivity is because of their electron structure and their band gap. In conductors there is no band gap, while in insulators there is a big band gap. However, the band gap in semiconductors is not as big as that found in insulators, and the band gap may change according to various conditions.

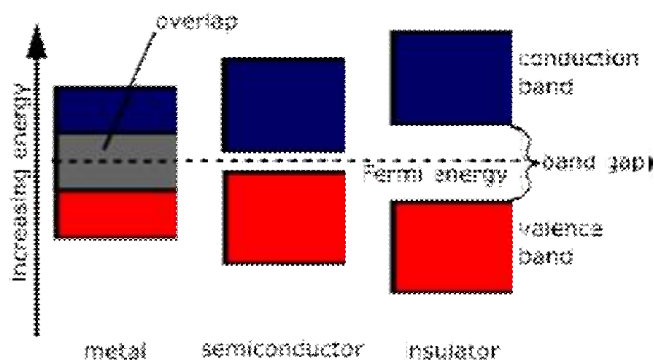


Figure 2.5 Band gap illustrations of metal, semiconductor and insulator [49].

Semiconductors resistivity is between conductors and insulators but more important property is resistivity can change according to temperature. Unlike conductors' resistivity, semiconductors' resistivity decreases with the increase of temperature. Further, by doping the semiconductor, the properties of the materials can be changed.

According to G.Busch, the term "semiconducting" was used for the first time by Alessandro Volta in 1782. The first documented observation of a semiconductor effect is that of Michael Faraday (1833), who noticed that the resistance of silver sulfide decreased with temperature, which was different than the dependence observed in metals." [50]

Semiconductor materials have been studied in laboratories from early as 1830. The first materials studied were elements and compounds, which are poor conductors if heated. However, when light is shone on semiconductors electrical current generated. This electrical current could pass through them in one direction only. This means we can control the direction of flow the electricity. Another example, radio receivers required a device called a rectifier to detect signals. Ferdinand Braun used the rectifying properties of the galena crystal, a semiconductor material composed of lead sulfide, to create the cat's whisker diode. The rectifying properties create a

voltage potential between the metal contact and the semiconductor such that electrons would ‘slide’ down the potential when going in one direction, but need to ‘climb’ up the potential in the opposite direction. Thus the first *semiconductor* device was produced. By 1874, electricity was being used not only to carry power, but also to carry information. The telegraph, telephone, and later the radio were the earliest devices in the industry that would eventually be called *electronics* [51]. And now almost every part of our life consists of semiconductors, from our cell phones, to the LEDs in our houses.

In 1878 Edwin Herbert Hall discovered that charge carriers in solids are deflected in magnetic field (The Hall Effect). This phenomenon was later used to study the properties of semiconductors. Shortly after the discovery of the electron by J.J. Thomson several scientists proposed theories of electron-based conduction in metals. The theory of Eduard Riecke (1899) is particularly interesting, because he assumed the presence of both negative and positive charge carriers with different concentrations and mobilities. Around 1908 Karl Baedeker observed the dependence of the conductivity of copper iodide on the stoichiometry (iodine content). He also measured the Hall effect in this material, which indicated carriers with positive charge [50].

Semiconductor elements are found between IIB and VIB groups in the periodic table.

The image shows a standard periodic table of elements. A red circle highlights the elements in groups III B, IV B, V B, and VI B, which are semiconductors. The table is color-coded: metals are blue, non-metals are yellow, and noble gases are red. The highlighted elements are: Al, Si, Ge, Sn, Pb, In, Ga, As, Sb, Bi, Te, Se, S, and O.

Periodic Table of the Elements																	
Metals										Non metals							
IA	IIA	d Transition Elements										III B	IV B	V B	VI B	VII B	VIII B
1 H	2 He	3 Li	4 Be	5 B	6 C	7 N	8 O	9 F	10 Ne	11 Na	12 Mg	13 Al	14 Si	15 P	16 S	17 Cl	18 Ar
19 K	20 Ca	21 Sc	22 Ti	23 V	24 Cr	25 Mn	26 Fe	27 Co	28 Ni	29 Cu	30 Zn	31 Ga	32 Ge	33 As	34 Se	35 Br	36 Kr
37 Rb	38 Sr	39 Y	40 Zr	41 Nb	42 Mo	43 Tc	44 Ru	45 Rh	46 Pd	47 Ag	48 Cd	49 In	50 Sn	51 Sb	52 Te	53 I	54 Xe
55 Cs	56 Ba	57 La*	72 Hf	73 Ta	74 W	75 Re	76 Os	77 Ir	78 Pt	79 Au	80 Hg	81 Tl	82 Pb	83 Bi	84 Po	85 At	86 Rn
87 Fr	88 Ra	89 Ac**	104 Unq	105 Unp	106 Uns	f Transition Elements											
* Lanthanides		58 Ce	59 Pr	60 Nd	61 Pm	62 Sm	63 Eu	64 Gd	65 Tb	66 Dy	67 Ho	68 Er	69 Tm	70 Yb	71 Lu		
** Actinides		90 Th	91 Pa	92 U	93 Np	94 Pu	95 Am	96 Cm	97 Bk	98 Cf	99 Es	100 Fm	101 Md	102 No	103 Lr		

Figure 2.6 The periodic table of the elements [52].

Semiconductor materials can be grouped in two: intrinsic semiconductors and extrinsic semiconductors.

2.2.1 Intrinsic Semiconductors

Semiconductors have two types of mobile charge carriers. One of these two is electron which is negatively charged so we denote these carriers by “n”. The other charge carrier is electron hole, electron hole simply means an electron left its position and left a hole behind it, as a negative charge left electron hole’s charge is positive and so we denote these carriers by “p”.

Intrinsic semiconductors are ideally perfect crystals. In an intrinsic semiconductor if an electron gets enough energy, it can go to the conduction band, and when electron goes to conduction band it leaves a hole behind. So we have an electron and a hole, and this is called “electron-hole pair creation”. For intrinsic semiconductors always holes created by moving of an electron to conduction band this means always number of negative charge carriers “n” is equal to positive charge carriers “p”.

2.2.2 Extrinsic Semiconductors

In the intrinsic semiconductors current may be induced with the movement of free charges but these current are very low to use them in practice. To use semiconductors we need significant currents so scientist tried to find a way to increase these currents, and which is possible with modification of the intrinsic property of the crystal lattice. Later this process has called doping. Doping process includes a specific number of atoms with a different valance number than the host semiconductor into crystalline lattice. With this modification semiconductor is no longer called intrinsic semiconductor, and it is called as extrinsic semiconductor. In extrinsic semiconductor number of charge carriers, electrons and holes, are not equal anymore. If the number of electrons is more than holes this means that semiconductor is "n-type" semiconductor, if the number of holes is more than electrons this means that semiconductor is "p-type" semiconductor.

An extrinsic semiconductor means it is a semiconductor which is doped and its electrical properties changed. Extrinsic semiconductors are used widely according to intrinsic semiconductor because by doping we can change the properties according to our needs.

2.2.3 Semiconductor Doping

Semiconductor doping is the process that changes an intrinsic semiconductor to an extrinsic semiconductor in order to produce a semiconductor with different electrical and optical properties. During this process we add appropriate atoms to the intrinsic semiconductor and this changes the concentration of electrons and holes. Dopant atoms can act in two different ways. They will either be donors or acceptors in the intrinsic semiconductor.

If the dopant atoms have more valence electrons than the atoms they replace in the intrinsic semiconductor, they donate their extra valence electrons to a semiconductor's conduction band, thereby giving excess electrons to the intrinsic semiconductor. Excess electrons increase the electron carrier concentration and which makes the number of negative charge carriers more than the positive charge carriers, so this type of semiconductor becomes "n-type semiconductor".

If the situation is the opposite, i.e., the dopant atoms have less valence electrons than the atoms they replace in the intrinsic semiconductor, they accept electrons from the semiconductor's valence band. This causes an increase in the concentration of the holes, and results in the number of positive charge carriers becoming more than the number of negative charge carriers, thereby producing a "p-type" semiconductor.

Whether an atom is a donor or an acceptor depends on its sequence of electrons, which is related to an atom's position in the periodic table. The column of the atom tells us if the atom is a donor or an acceptor.

Group IV semiconductors use Group V atoms as donors and Group III atoms as acceptors. Group III-V semiconductors, the compound semiconductors, use Group VI atoms as donors and Group II atoms as acceptors. Group III-V semiconductors can also use Group IV atoms as either donors or acceptors. When a Group IV atom replaces the Group III element in the semiconductor lattice, the group IV atom acts as a donor. Conversely, when a Group IV atom replaces the Group V element, the Group IV atom acts as an acceptor. Since Group IV atoms can act as both donors and acceptors, they are known as amphoteric impurities [53].

Table 2.2 Semiconductor donors, and acceptors [53].

	Intrinsic semiconductor	Donor atoms	Acceptor atoms
Group IV semiconductors	Silicon, Germanium	Phosphorus, Arsenic	Boron, Aluminium
Group III-V semiconductors	Aluminum phosphide, Aluminum arsenide, Gallium arsenide, Gallium nitride	Selenium, Tellurium, Silicon, Germanium	Beryllium, Zinc, Cadmium, Silicon, Germanium

Extrinsic semiconductors are two types; N-Type and P-Type.

2.2.4 N-Type Semiconductors

An n-type semiconductor is produced by adding a donor impurity such as arsenic, antimony, or phosphorus to an intrinsic semiconductor. Each donor atom has five valence electrons. When a donor atom replaces an atom in the crystal lattice, only four valence electrons are shared with the surrounding atoms. The fifth valence electron becomes a free electron as illustrated in figure 2.8. The number of free electrons donated by the donor atoms is much greater than the number of free electrons and holes in the intrinsic semiconductor. Because the number of free electrons is far greater than the number of holes, the electrons are the majority carriers. The semiconductor is called n-type because the majority carriers have a negative charge.

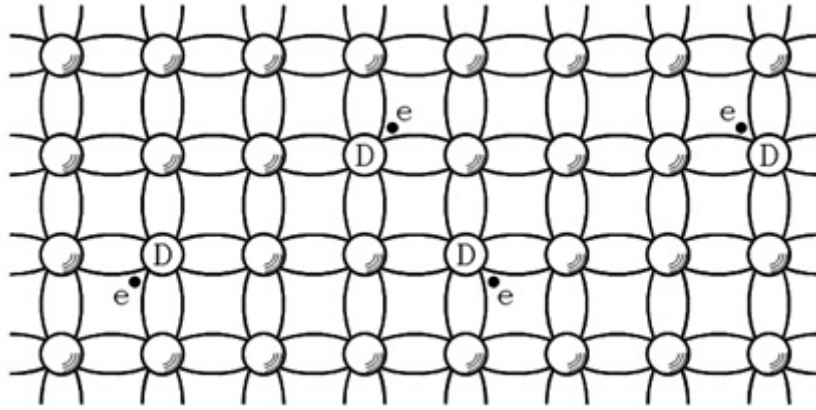


Figure 2.7 Two-dimensional illustration of the crystal lattice of an n-type semiconductor [52].

Hole-electron pairs are continually formed by thermal agitation of the lattice in an n-type semiconductor. Because of the large number of donor electrons, there are many more free electrons available for recombination with the holes. This decreases the mean lifetime for the holes, which in turn decreases the number of holes in the n-type semiconductor compared to the intrinsic semiconductor. For this reason, the current due to the flow of holes in an n-type semiconductor is often neglected in calculations [52].

2.2.5 P-Type Semiconductor

A p-type semiconductor is produced by adding an acceptor impurity such as gallium, boron or indium to an intrinsic semiconductor. Each acceptor atom has three valence electrons. When an acceptor atom replaces an atom in the crystal lattice, only three valence electrons are shared with the surrounding atoms. This leaves a hole as illustrated in figure 2.9. The number of holes created by the acceptor atoms is much greater than the number of free electrons and holes in the intrinsic semiconductor. This makes the conductivity of the p-type semiconductor much greater than that of the intrinsic semiconductor. Because the number of holes is far greater than the number of electrons, holes are the majority carriers. The semiconductor is called p-type because the majority carriers have a positive charge.

Hole-electron pairs are continually formed by thermal agitation of the lattice in a p-type semiconductor. Because of the large number of holes, there are many more holes available for recombination with the free electrons. This decreases the mean

lifetime for the free electrons which in turn decreases the number of electrons in the p-type semiconductor compared to the intrinsic semiconductor. For this reason, the current due to the flow of free electrons in a p-type semiconductor is often neglected in calculations [52].

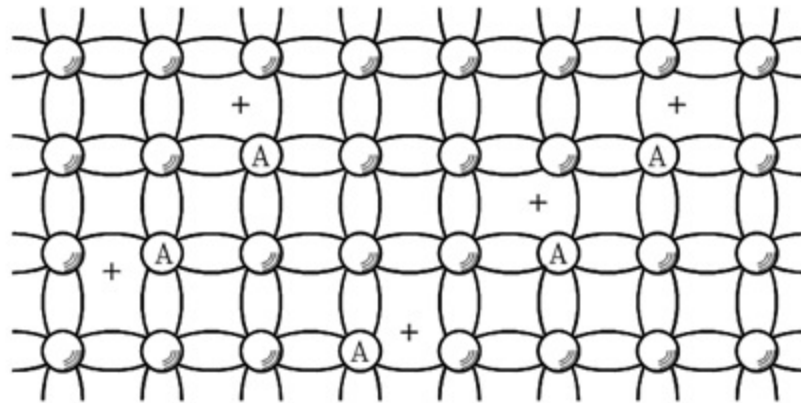


Figure 2.8 Two-dimensional illustration of the crystal lattice of a p-type semiconductor [52].

2.3 Optical Transition

Transition refers to the transition of an electron from the valance band to the conduction band. In semiconductors there are two types of transition: direct transition and indirect transition.

If the lowest value between the valence band and conduction band takes place at $k=0$, we call these kind of semiconductors direct band gap semiconductors. Transitions occur directly in these semiconductors.

If the lowest value between the valence band and conduction band takes place other than $k=0$, which means $k \neq 0$, we call these kind of semiconductors indirect band gap semiconductors. In these kinds of semiconductors, transition it occurs indirectly. Direct transition is not possible because the electron has to change its direction which requires a momentum change. A phonon does this job. A phonon changes electron's direction and so electron can go to conduction band. As it is done not directly we call this transition indirect transition.

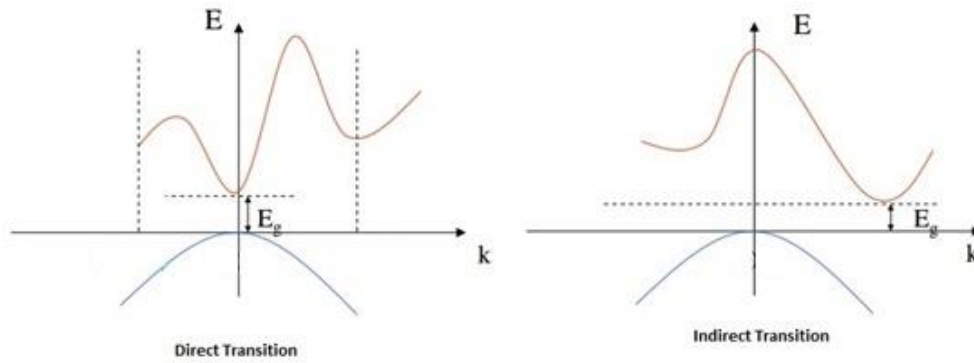


Figure 2.9 Band gap illustration of direct transition and indirect transition [54].

Direct transition occurs with a photon. If a photon has equal or greater energy than the energy difference between the conduction band and valence band, which is also called band gap energy, an electron can absorb this energy from the photon and can go to conduction band. During the transition both momentum and energy are conserved.

We can determine whether a band gap is direct or indirect by absorption spectroscopy. We use the absorption coefficient for this process.

The absorption coefficient, α , for a direct band gap is;

$$\alpha \approx A^* \sqrt{h\nu - E_g}, \quad (2.18)$$

$$A^* = \frac{q^2 x_{vc}^2 (2m_r)^{3/2}}{\lambda_0 \epsilon_0 \hbar^3 n} \quad (2.19)$$

with

where:

- α is the absorption coefficient, a function of light frequency
- ν is light frequency
- h is Planck's constant ($h\nu$ is the energy of a photon with frequency ν)
- \hbar is reduced Planck's constant ($\hbar = h/2\pi$)
- E_g is the band gap energy
- A^* is a certain frequency-independent constant, with formula above

$$m_r = \frac{m_h^* m_e^*}{m_h^* + m_e^*} \quad (2.20)$$

where m_e^* and m_h^* are the effective masses of the electron and hole, respectively (m_r is called a "reduced mass")

- q is the elementary charge
- n is the (real) index of refraction
- ϵ_0 is the vacuum permittivity
- x_{vc} is a "matrix element", with units of length and typical value the same order of magnitude as the lattice constant. [55]

The absorption coefficient, α , for indirect band gap is;

$$\alpha \propto \frac{(h\nu - E_g + E_p)^2}{\exp(E_p / kT) - 1} + \frac{(h\nu - E_g + E_p)^2}{1 - \exp(-E_p / kT)} \quad (2.21)$$

where:

- E_p is the energy of the phonon that assists in the transition
- k is Boltzmann's constant
- T is the thermodynamic temperature [55]

2.3.1 Optical Absorption

Optical absorption is the process by which the energy of a photon (electromagnetic energy) is taken by a particle, such as an electron. Through optical absorption this electromagnetic energy is turned into internal energy of the particle that absorbs the energy.

Beer-Lambert law states that there is a logarithmic dependence between transmission, absorption and the distance the light travels through the material. They found the following equation;

$$-\frac{dI_x}{I_x} = \frac{\sigma CA}{A} dx \quad (2.22)$$

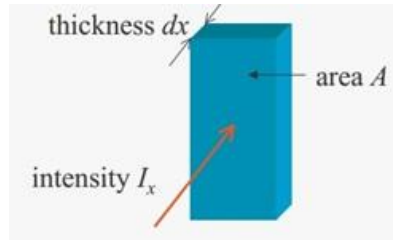


Figure 2.10 Three dimensional solid matter

where dI_x is the change in intensity across dx .

If we integrate both sides

$$\int_{I_0}^I \frac{dI_x}{I_x} = -\int_0^x \sigma C dx \quad (2.23)$$

$$\ln(I) - \ln(I_0) = \ln \frac{I}{I_0} = -\sigma C x \quad (2.24)$$

$$I = I_0 e^{-\sigma C x} = I_0 e^{-\mu x} \quad (2.25)$$

The coefficient $\mu = \sigma C$ is the linear attenuation coefficient. [56]

The optical absorption process is very useful in the calculation of the band gap. If we send photons to an atom, the photons that have an equal or greater energy than the band gap of the atom will be absorbed. If we send to the atom, photons have less energy than the band gap; these photons cannot help the electrons to go to the conduction band. The photons will not be absorbed but they will be transmitted. Thus by this process one can determine the band gap of the atom.

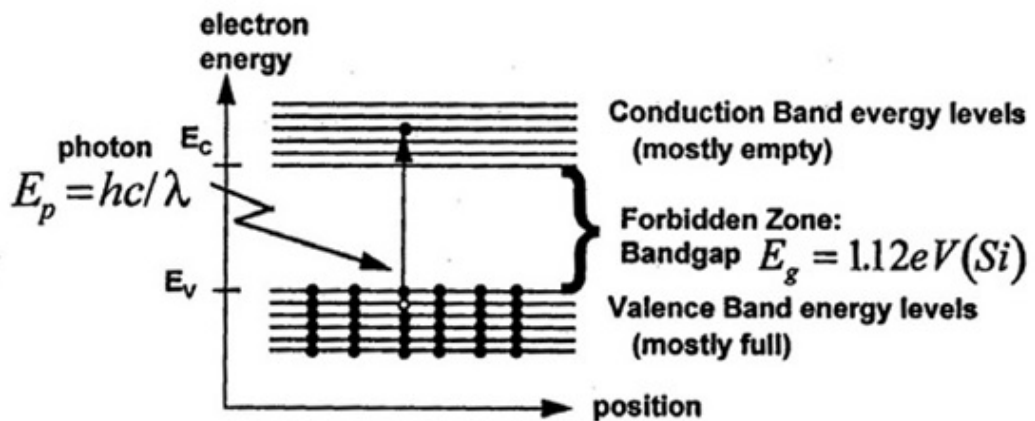


Figure 2.11 Optical absorption in a semiconductor [57].

2.4 X-Ray Diffraction Method

The electromagnetic spectrum is currently divided into seven groups; radio waves, microwaves, infrared, visible light, ultraviolet, x-rays, and gamma rays, where radio waves represent the biggest wavelengths, while gamma rays represents the smallest. There is an inverse ratio between the wavelength and frequency of a photon, and also between the wavelength and energy of the photon. These mean X-rays have the second biggest frequency and energy in the electromagnetic spectrum and the second smallest wavelength.

X-rays' wavelength is between 0.01 and 10 nanometers, and its frequency is between 3×10^{16} Hz and 3×10^{19} Hz, which corresponds to the energy between 120 eV to 120 keV.

X-rays were discovered by Wilhelm Conrad Rontgen, who coined the term "X-rays" because these rays were unknown.

We produce X-rays in X-ray tubes, where there is a cathode that emits electrons and an anode which collects the electrons. This causes an electric current that is actually a beam. If we connect a high voltage power source we can accelerate the electrons to produce X-rays.

X-rays are used to get information with X-ray diffraction. X-ray diffraction is very important and useful because it is non-destructive and it gives crystal structure, chemical composition and physical properties of thin films. In X-ray diffraction Bragg's law is valid.

We can derive Bragg's law like;

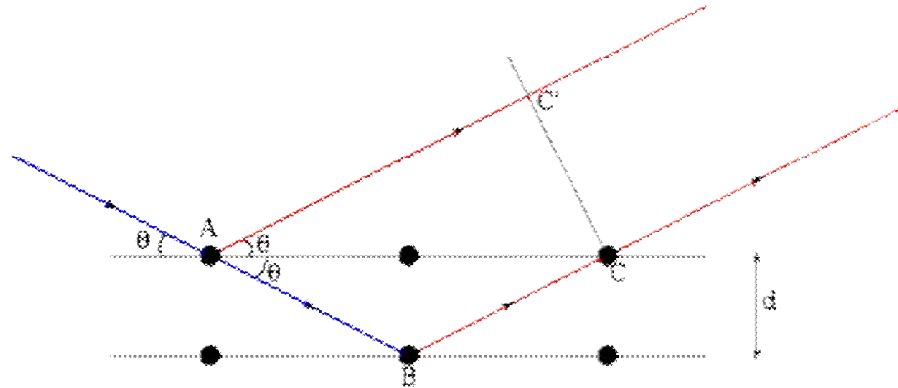


Figure 2.12 Path difference of reflected ray and transmitted then reflected ray [58].

There will be a path difference between the ray that gets reflected along AC' and the ray that gets transmitted, and then reflected, along AB and BC respectively. This path difference is

$$(AB+BC)-(AC') \quad (2.26)$$

The two separate waves will arrive at a point with the same phase, and hence undergo constructive interference, if, and only if, this path difference is equal to any integer value of the wavelength, i.e.

$$(AB+BC)-(AC')=n\lambda, \quad (2.27)$$

where the same definition of n and λ apply as above.

Therefore,

$$AB=BC=\frac{d}{\sin\theta} \quad (2.28)$$

$$AC=\frac{2d}{\tan\theta}, \quad (2.29)$$

$$AC'=AC \cdot \cos\theta = \frac{2d}{\tan\theta} \cos\theta = \left(\frac{2d}{\sin\theta} \cos\theta\right) \cos\theta = \frac{2d}{\sin\theta} \cos^2\theta \quad (2.30)$$

$$n\lambda = \frac{2d}{\sin\theta} (1-\cos^2\theta) = \frac{2d}{\sin\theta} \sin^2\theta, \quad (2.31)$$

$$n\lambda = 2d\sin\theta, \quad (2.32)$$

which is Bragg's law [58].

The main goal of X-ray crystallography is to determine the density of electrons $f(\mathbf{r})$ throughout the crystal, where \mathbf{r} represents the three-dimensional position vector within the crystal. To do this, X-ray scattering is used to collect data about its Fourier transform $F(\mathbf{q})$, which is inverted mathematically to obtain the density defined in real space, using the formula

$$f(\mathbf{r}) = \frac{1}{(2\pi)^3} \int F(\mathbf{q}) e^{i\mathbf{q}\cdot\mathbf{r}} d\mathbf{q} \quad (2.33)$$

where the integral is taken over all values of \mathbf{q} . The three-dimensional real vector \mathbf{q} represents a point in reciprocal space, that is, to a particular oscillation in the electron density as one moves in the direction in which \mathbf{q} points. The length of \mathbf{q} corresponds to 2π divided by the wavelength of the oscillation. The corresponding formula for a Fourier transform will be used below

$$F(\mathbf{q}) = \int f(\mathbf{r}) e^{-i\mathbf{q}\cdot\mathbf{r}} d\mathbf{r} \quad (2.34)$$

where the integral is summed over all possible values of the position vector \mathbf{r} within the crystal.

The Fourier transform $F(\mathbf{q})$ is generally a complex number, and therefore has a magnitude $|F(\mathbf{q})|$ and a phase $\phi(\mathbf{q})$ defined by the equation

$$F(\mathbf{q}) = |F(\mathbf{q})| e^{i\phi(\mathbf{q})} \quad (2.35)$$

The intensities of the reflections observed in X-ray diffraction give us the magnitudes $|F(\mathbf{q})|$ but not the phases $\phi(\mathbf{q})$. To obtain the phases, full sets of reflections are collected with known alterations to the scattering, either by modulating the wavelength past a certain absorption edge or by adding strongly scattering (i.e., electron-dense) metal atoms such as mercury. Combining the magnitudes and phases yields the full Fourier transform $F(\mathbf{q})$, which may be inverted to obtain the electron density $f(\mathbf{r})$.

Crystals are often idealized as being *perfectly* periodic. In that ideal case, the atoms are positioned on a perfect lattice, the electron density is perfectly periodic, and the Fourier transform $F(\mathbf{q})$ is zero except when \mathbf{q} belongs to the reciprocal lattice (the so-called *Bragg peaks*). In reality, however, crystals are not perfectly periodic; atoms vibrate about their mean position, and there may be disorder of various types, such as

mosaicity, dislocations, various point defects, and heterogeneity in the conformation of crystallized molecules. Therefore, the Bragg peaks have a finite width and there may be significant *diffuse scattering*, a continuum of scattered X-rays that fall between the Bragg peaks.

2.5 Scanning Electron Microscope Measurement

The electron microscope, which uses a beam of electron, was constructed by Ernst Ruska in 1933. Electrons have a much shorter wavelength than visible light, and this enables the electron microscope to magnify the images much more than light microscope. The first prototype of the electron microscope was a transmission electron microscope, but later more types were invented, such as the scanning electron microscope, the reflection electron microscope and the scanning transmission electron microscope.

The light microscope has magnification ability about 1000x times, but the electron microscope has magnification ability more than about 1000000x, so electron microscope is a much more sensitive instrument to use.

The Scanning Electron Microscope produces an image of the sample by scanning the sample with an electron beam. The Scanning Electron Microscope is the most widely used among the electron microscope types, because, it has many advantages. For example, the scanning electron microscope doesn't use lenses, but it uses electromagnets which make controlling magnification easier. Another great advantage of the scanning electron microscope is that unlike the transmission electron microscope, it uses electron interactions at the surface. This enables the scanning electron microscope to have a greater depth of view so that we can have a good representation of the 3D structure of the sample.

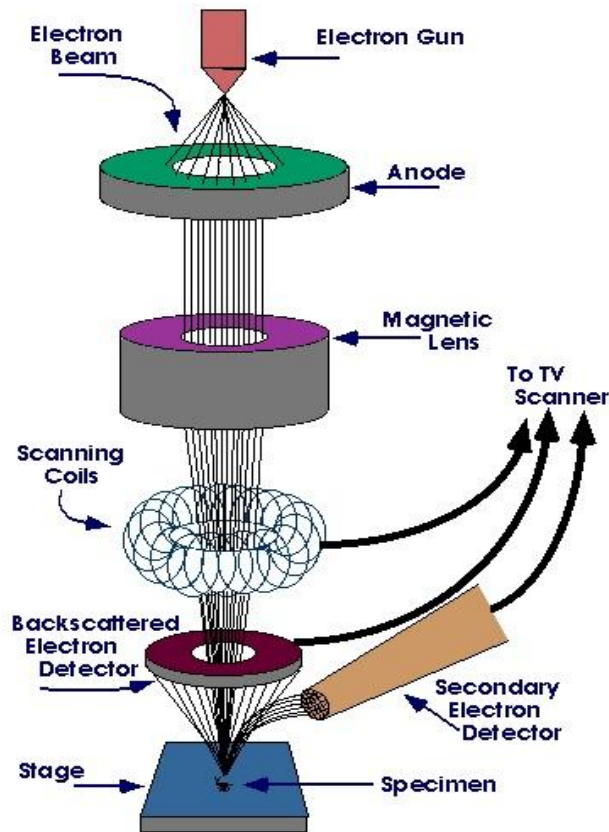


Figure 2.13 Basic parts of SEM [59].

As we can see in the figure the main parts of a scanning electron microscope are the electron gun, anode, magnetic lenses, scanning coils, backscattered electron detector, secondary electron detector, and a monitor. Additionally, since the medium must be vacuum, there is a vacuum pump.

An Electron Beam comes from the electron gun, passes through the electromagnets and scanning coils, and falls onto a specimen. Instead of lenses, we use an electromagnet for focusing the electron beam. When the electron beam falls onto the specimen, we get X-rays, auger electrons, primary backscattered electrons and secondary electrons. Detectors collect these, and then convert them into signals. These signals are then sent to a monitor where the image is visible. The most important signal is from the secondary electrons because these provide information about the morphology and topography of the sample. The secondary electron comes out when an electron from the beam hits an electron from the sample and removes it from its shell; we call this displaced electron a secondary electron.

The resolution of the microscope depends on the energy of the electrons in the following way;

$$\text{DeBroglie wavelength} \quad \lambda = \frac{h}{mv} \quad (2.36)$$

where

λ : wavelength

h: Planck constant

m: mass of particle

v: velocity of the particle

For electron passes through the potential field

$$\lambda = \frac{h}{mv} = \frac{h}{\sqrt{2qmV}} \quad (2.37)$$

$$\lambda = \frac{1.23}{\sqrt{V}} \text{nm} \quad (2.38)$$

where

V: accelerating potential

q: charge of electron

m: mass of electron

$$\text{Abbe's equation is} \quad d = \frac{0.61\lambda}{n \sin \alpha} \quad (2.39)$$

For electron microscopes $n \approx 1$ and $n \sin \alpha \approx \alpha$

where α is the half opening angle of objective in radians

$$d = \frac{0.753}{\alpha \sqrt{V}} \text{ (nm)} \quad (2.40)$$

The voltage on the scanning electron microscope is between 1 and 30 kV, so the effective instrument resolution is about 1 nm.

CHAPTER 3

EXPERIMENTAL STUDIES

3.1 Spray Pyrolysis Method

The Spray Pyrolysis method, also known as solution spraying, is a type of chemical vapour deposition. This method is widely used in semiconducting thin and thick film growth. This method is widely used because it is easy to use and does not need too many tools. In our study, we used air to atomize the solution but there are other types of spray pyrolysis that depend on the technique used to atomize the solution, such as; ultrasonic nebulisation, improved spray hydrolysis, corona spray pyrolysis, electrostatic spray pyrolysis and microprocessor based spray pyrolysis.

The Spray Pyrolysis method is based on spraying an atomized solution onto a heated substrate. In this method there are several important parameters which affect the quality and properties of the film. The most important parameters are:

1. Properties of substrate
2. Temperature of substrate
3. Spraying nozzle
4. Uniformity of the droplet size of solution
5. Flow rate of spraying solution
6. Distance and place of nozzle to substrate surface

The temperature of the substrate and interval of spraying are easily controlled by a thermostat system and control panel. However, the chemical composition must be carefully chosen because chemicals in the solution should provide a thermally activated chemical reaction to yield the desired film material, and the remainder of the constituents, including the carrier liquid should be volatile at the substrate temperature. The nozzle should be placed about 20 cm away from the substrate. In our experimental set up, we placed the nozzle to spray at an angle because our nozzle

leaves some liquid drops. So, in order to avoid harming the growth of film, we could not place the substrate directly under the nozzle.

3.1.1 Experimental Setup

In this study, we used the spray pyrolysis technique for film growth Figure 3.1 shows a basic schematic diagram of our experimental setup. The experimental setup consists of the air pump, control panel, heater, nozzle, solution container, thermostat and glass chamber.

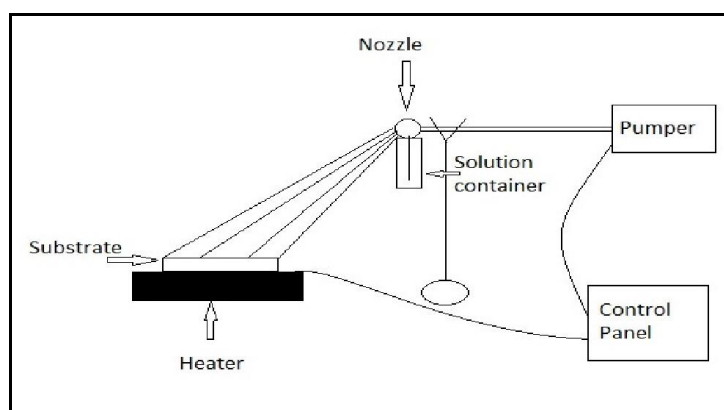


Figure 3.1 Experimental setup of spray pyrolysis method

Heater: The substrate temperature, which is very important for film growth, was changed by the heater. We controlled the temperature of the heater from the control panel. There is a thermostat that controls the temperature of the heater and maintains the temperature at predetermined setting with an accuracy of $\pm 5^{\circ}\text{C}$. The power of the heater is 2500 watts and it operates at 220 volts and 50 Hertz (AC).

Air Pump: This device is used to atomize the prepared solution and spray onto the heated substrate by pumping air. We controlled the time interval of the air pump from the control panel.

Nozzle: Due to the help of pumped air, the solution becomes atomized and sprayed from the nozzle to the desired area on the heated substrate.

3.1.2 Substrate Preparation

In this study, we used glass lamella as substrates. The crystalline films are suitable grown on an amorphous material so that we used a glass lamella substrate as an

amorphous materials. Other reasons for using lamella that it is easy to find in stores, it is cheap, and transparent. We took ordinary lamella and cut it into smaller parts approximately 0, 5 cm² surface area. Generally, we took 3 or 4 of these glass particles in case some were lost or broken during the experiment or later during measurements. Before placing the glass substrate on the heater, they were cleaned as defined; Firstly, all of them were washed with distilled water for some dust residues, they were then dried. Secondly, we cleaned them with methyl alcohol. The purpose of putting the substrates in methyl alcohol was to remove any oily substances. After drying the substrates, we cleaned them with isopropyl alcohol, and dried them. The purpose of cleaning with isopropyl alcohol was to remove any dust and tiny particles. Finally we cleaned them with distilled water again and dried them again. During the entire process we used tweezers and we did not touch them directly. After this cleaning process, our substrates were ready to use as substrate.

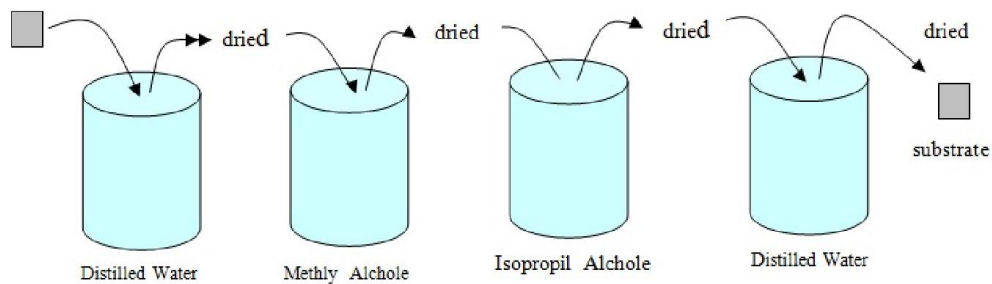


Figure 3.2 Cleaning process of substrate

3.1.3 Solution Preparation

In this study, we prepared two types of solutions, one of them to produce MnO and the other to produce boron doped MnO. In both cases, we used a high sensible electronic balance which can measure the mass of the chemicals with $\pm 0, 5$ mg accuracy. During this study, we always poured the chemicals into 100 ml of distilled water. After we poured the chemical into distilled water, we mixed them using a magnetic mixer.

3.1.4 Development of MnO Films

After preparation of the substrate and solution, we set the temperature and pumping interval. When the substrate reached the arranged temperature the pumper started to

pump air at the set time intervals. High speed air, which means it has low pressure, atomizes the solution while it passes above it, and with the help of nozzle, atomized solution particles were sprayed onto heated substrates. When the solution in the container finished, our films were ready.

In this study, we first prepared solutions to get MnO films. To get MnO films we used manganese chloride (MnCl_2) as a Mn^+ ion source at 1 M concentration in 100 ml deionized water, was an O^- ion source. We did the experiment at the temperatures 325°C , 350°C , 375°C and 400°C . After doing these experiments, we observed that the most appropriate temperature for growth of MnO films is at 375°C . The carrier gas flow rate was $5\text{dm}^3\text{ min}^{-1}$ and the solution flow rate was $5\text{ cm}^3\text{ min}^{-1}$. Air was used to atomize the spray. Consistent conditions of substrate temperature and flow rate of carrier gas were maintained during deposition of such films. The formation of MnO resulted from the chemical reaction,



3.1.5 Development of Boron Doped MnO Films

The process of developing boron doped MnO films was similar to with the process used to develop MnO films. We kept all of the parameters the same except that we added another chemical, boric acid. Boron-doping was achieved by adding different molarities (0.1, 0.2, 0.3 and 0.4 M, respectively) H_3BO_3 into the starting solution, which included manganese chloride (MnCl_2) at 1 M concentration in 100 ml deionized water. We did the experiment at the temperatures 325°C , 350°C , 375°C and 400°C . After doing these experiments we saw that 375°C is the most appropriate temperature for the growth of boron doped MnO films and took these samples for measurements. The carrier gas flow rate was $5\text{dm}^3\text{ min}^{-1}$ and the solution flow rate was $5\text{ cm}^3\text{ min}^{-1}$. Air was used to atomize the spray. Consistent conditions of substrate temperature and flow rate of carrier gas were maintained during deposition of such films. The formation of boron doped MnO resulted from the chemical reaction,



The desired semiconductor compound formed on the substrate and the remaining component evaporated upon quaring at $T=375^\circ\text{C}$.

CHAPTER 4

RESULTS and DISCUSSION

4.XRD Analysis of MnO and Boron doped MnO films

4.1 Introduction

X-ray powder diffraction (XRD) is a rapid analytical technique primarily used for phase identification of a crystalline material and can provide information on unit cell dimensions. X-ray powder diffraction is most widely used for the identification of unknown crystalline materials (e.g. minerals, inorganic compounds). X-ray diffraction is based on constructive interference of monochromatic X-rays and a crystalline sample. These X-rays are generated by a cathode ray tube, filtered to produce monochromatic radiation, collimated to concentrate, and directed toward the sample. The interaction of the incident rays with the sample produces constructive interference (and a diffracted ray) when conditions satisfy Bragg's Law,

$$n\lambda=2d \sin \theta \quad (5.1)$$

This law relates the wavelength of electromagnetic radiation to the diffraction angle and the lattice spacing in a crystalline sample [60]

4.2 Crystal Structural studies

X-ray diffraction pattern was recorded on diffractometer (X-ray diffraction (XRD) measurements were performed on a PANalytical X'Pert diffractometer using $\text{CuK}\alpha$ radiation with a wavelength $\lambda=1.5410 \text{ \AA}$ at 2θ values between 20° and 80° . Boron doped MnO films were deposited on highly clean glass substrates (about 0.5 cm^2 of geometric area) at the constant substrate temperature $T=375^\circ\text{C}$ by using spray pyrolysis technique. The initial solution was prepared from 1.0 M magnesium chloride (MnCl_2) as a Mn-ion source in 100 ml of deionized water. Boron-doping was achieved by adding 0.1M, 0.2M, 0.3M and 0.4M H_3BO_3 to the starting solution. The structural evaluation of MnO film was shown in Figure 4.1 and Table 4.1. The

diffraction pattern exhibit peaks at $2\theta=28.4098^\circ$, $2\theta=47.2858^\circ$ and $2\theta=56.0638^\circ$ were identified to be (111), (220) and (311) planes having cubic structure with lattice parameter, approximately, $a=5.4\text{\AA}$ which is in agreement with literature value of 4.445\AA [61].

X-ray diffraction (XRD) pattern of MnO:B films prepared by spraying pyrolysis method is shown in Figure 4.1. It indicates that most of the grains in MnO:B films have a strong orientation along (111) and (220) planes as seen in Figure 4.1. While the intensity of (111) and (220) peaks are increasing with increasing boron concentration up to 0.1M and then the intensity of (111) and (220) peaks are decreasing with increasing boron concentration from 0.2M to 0.4M. This behaviour can be understood by two competing processes; the increase in boron doping improves the stoichiometry of the films and the crystal quality. This indicates that boron ions are substituted at manganese ions sites up to 0.1M after that B-B intragrain cluster is evaluated. XRD pattern of highly boron doped (from 0.2M to 0.4M) MnO films is shown in Figure 4.1 and the inset shows the B-B cluster intragrain. It is observed that the XRD intensity depends strongly on the boric acid concentrations. The maximum of the XRD intensity is illustrated by the pronounced peak at a boric acid concentration of 0.1M. Thus, increasing the dopant level results in a change in preferred growth (111) and (220) direction. The spray deposition of 0.1M boron doped MnO films deposited at a substrate temperature of 375°C is found to be optimum for the deposition of good quality boron doped MnO films at the specified spray conditions. It is shown that there is a critical doping value in the starting solution for which the characteristics of the boron doped MnO films has a minimum value, corresponding to the maximum crystal grain size value measured for these films. Consequently, the characteristics of boron doped MnO films prepared by the spray pyrolysis process depend strongly on the boron incorporation at the films. A similar behavior has already been observed by Pawar et al. [26]. It is also shown in Figure 4.1 that the initial increase in the XRD peaks can be explained by the creation of new nucleating centers due to the B dopant atoms. The subsequent decrease in the XRD peaks for the high doping level could be explained by two factors; firstly, by the saturation of the newer nucleating centers and secondly, due to the change in the energy absorption at the time of collision, and of the physical and chemical interaction between ad atoms and the film. For boron doped films, the grain

size initially increases with an increase in dopant contents (up to 1.0M). Then, there is a decrease in the crystal grain size with the increase in the boric acid concentrations, which may be due to the sufficient increase in the supply of thermal energy for re-crystallization. This trend suggests that boron dopant creates newer nucleation centers, which in turn, would change the nucleation type from homogeneous to heterogeneous, and deteriorate the crystalline structure at high doping level.

As the following observations have been made from the X-ray diffraction spectra:

1. The X-ray reflection peaks at different planes indicate that films are polycrystalline over the whole range of boron doping concentration studied. The intensity of peaks and crystal orientations are influenced by the boron doping concentration.
2. The registered X-ray spectra fit to a MnO cubic structure [61] without any new reflections. No additional peaks of MnO phases and the traces of either B or Mn metals have been observed. This indicates that the B are substituted at Mn sites without changing the MnO structure.

It is also observed that the addition of boric acid contents increases the full width at half maximum (FWHM) due to the destruction of the crystal structure and reduction in the grain size. It may be possible that this drastic change in grain size is due to the large difference in ionic radius of manganese and boron.

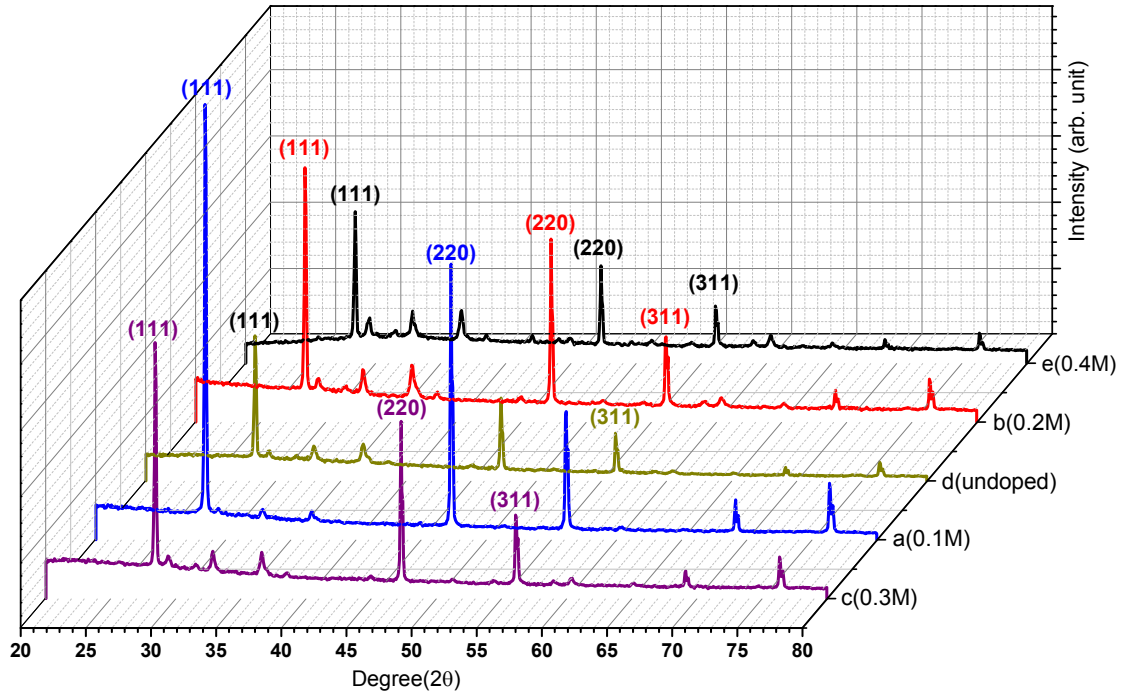


Figure 4.1 XRD patterns of undoped and boron doped MnO films with the different concentrations of boric acid in the starting solution; (a) 0.1 M, (b) 0.2 M, (c) 0.3 M, (d) undoped, (e) 0.4 M.

4.3 Lattice Constant (a) Studies

The lattice constant, or lattice parameter, refers to the physical dimension of unit cells in a crystal lattice. Lattices in three dimensions generally have three lattice constants, referred to as a , b , and c . However, in the special case of cubic crystal structures, all of the constants are equal and only refer to a . The lattice constant ‘ a ’ for the cubic phase structure is determined by the relation

$$a^2 = \lambda^2(h^2 + k^2 + l^2)/4\sin^2 \theta \quad (5.2)$$

where θ is the diffraction spectra (Bragg’s angle), λ is the wavelength of the X-ray [62]. Lattice parameters for the undoped and boron doped MnO films are calculated using the relevant formula and systematically represented in Table 4.1. The variation of the lattice constant with molar ratio of the boron doping on the MnO films are shown in Table 4.1. The lattice constant ‘ a ’ first decreases, reaches a minimum value around undoped MnO film and then appears to slowly increase with increasing of the

boron doped around the 5.3 and 5.4Å⁰ as shown in Table 4.1. The slowly change in lattice constant for the spray deposited boron doped MnO film over the bulk clearly suggests that the film grains are strained which may be due to the nature and concentration of the native imperfections changing. The variation of the molar ratio of the boron in the MnO associated with the changes in grain size and boundary.

4.4 Grain Size Studies

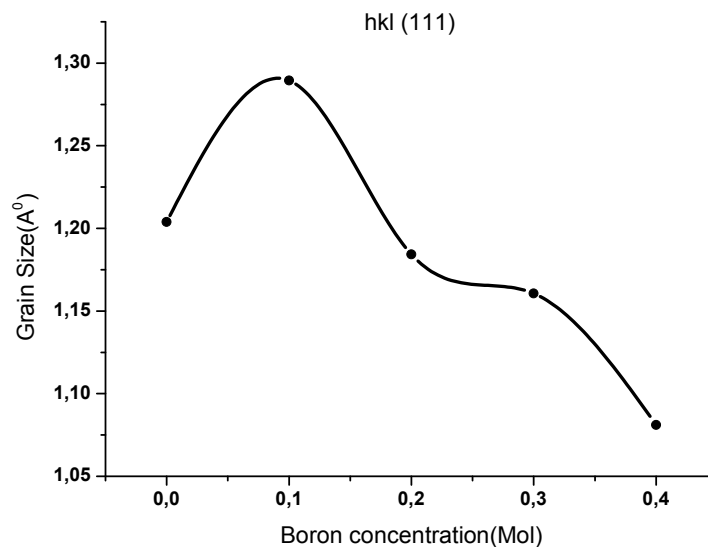
It is observed that the XRD patterns of the undoped and boron doped MnO films show a most preferred orientation along (111), (220) and (311) plane. The grain size all of the films were estimated for the planes by using the Scherrer formula [19].

$$d = \lambda / D \cos \theta \quad (5.3)$$

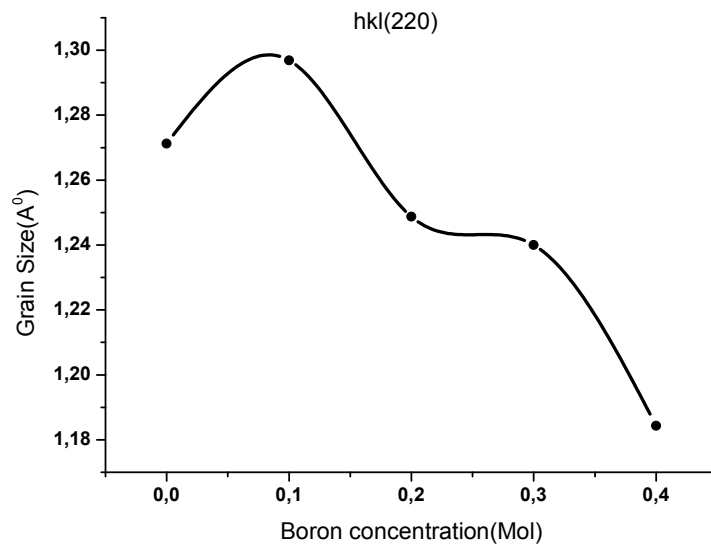
where d is the grain size, λ is the X-ray wavelength used, D is the angular line width of the half maximum intensity and θ is the Bragg angle [63]. Table 4.1, Figure 4.2(a), (b) and (c) show the various grain parameters of the undoped and boron doped MnO films which is associated to the (111), (220) and (311) peaks. From these results, the boron concentration increases to 0.1M concentration the intensity of MnO peaks increases and this peak becomes narrower indicating an improvement of the crystallinity. This means that the grain size of the films increases with increasing up to 0.1 M concentration of the boric acid. Then the boron concentration increases 0.2M to 0.4M concentration of the boric acid the intensity of MnO peaks decreases and this peak becomes larger due to the destruction of the crystal structure and reduction of the grain size. The XRD intensity depends strongly the boron concentration permitted for maximum XRD intensity is illustrated by the pronounced peak with dopant contents (0.1M concentration of boric acid). It is shown that the decrease in the grain size is correlated with the broadening of the XRD peak. Smaller crystallite size results in a higher density of grain boundaries, which behaves as barriers for carrier transport and traps for free carrier. Hence, a decrease in the crystallite size can cause an increase in the grain boundary scattering [64,65]. This observations correlates with the results of XRD patterns. Consequently, the characteristics of the undoped and boron doped MnO films prepared by the spray pyrolysis process depend strongly to the boron incorporation at the films. It is also shown in Figure 4.2 that the initial increase in the XRD peaks can be explained by

the creation of new nucleating centers due to the B dopant atoms. The subsequent decrease of the XRD peaks for the higher doping level could be explained by two factors; firstly, by the saturation of the newer nucleating centers and secondly, due to the change of the energy absorption at the time of collision, and of the physical and chemical interaction between ad-atoms and the film. Thus, it is observed that the grain size initially increases with an increase in dopant contents (up to 0.1M). Then, the grain size of these films decreases for higher doping level. This trend suggests that B dopant creates newer nucleation centers, which in turn, would change the nucleation type from homogeneous to heterogeneous, and deteriorate the crystalline structure at higher doping level.

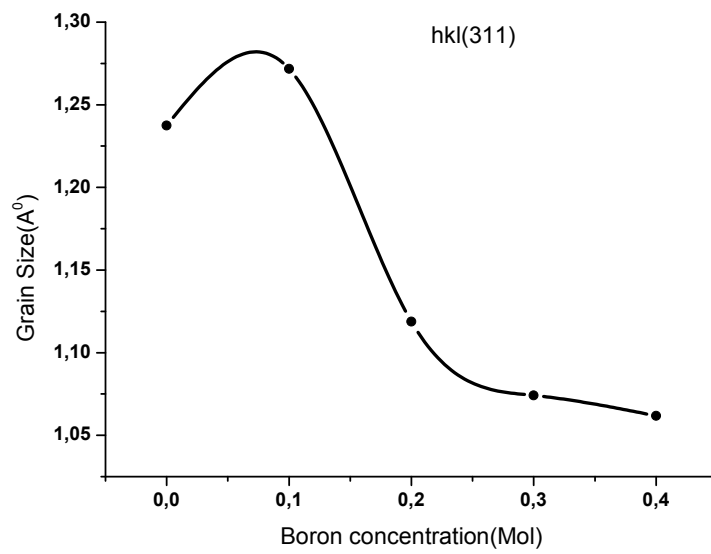
It is concluded that the crystallinity of the films increase with increase in grain size, which indicates a lower number of lattice imperfections. This may be due to a decrease in the occurrence of grain boundaries because of an increase on the grain size of the film with increase of boron concentration up to 0.1M concentration of boric acid. These parameters indicate the formation of high quality B-MnO films deposited on the well cleaned glass substrate by spraying pyrolysis method with dopant contents (up to 0.1M).



(a)



(b)



(c)

Figure 4.2. Variation of the grain size (d) with different boron concentration in MnO films

4.5 Microstrain studies

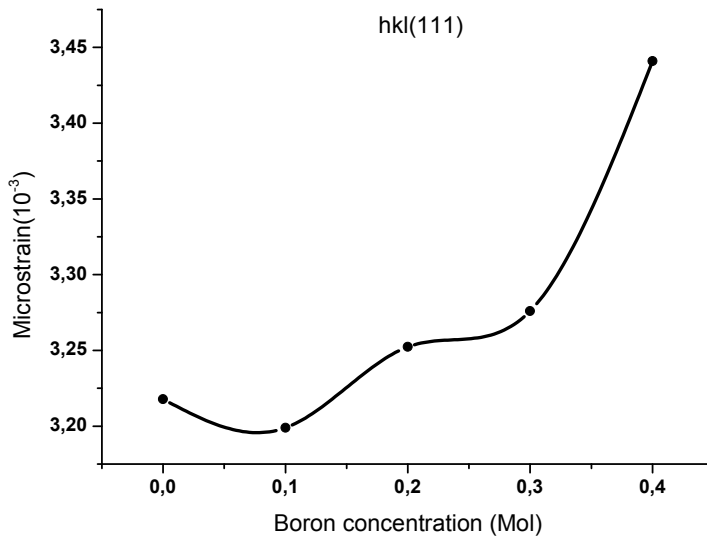
Misfit stresses occur in crystalline films due to the geometric mismatch at interphase boundaries between crystalline lattices of films and substrate. Therefore, a stress is also developed in the film due to the lattice misfit [66,67]. However, the stress has two components: thermal stress arising from the difference of expansion coefficient of the film and substrate and internal stress due to the accumulating effect of the crystallographic flaws that are built into the film during deposition [68]. The average stresses of the deposited films are found to be compressional in nature. The compressive stress is due to the grain boundary effect, which is predominant in polycrystalline film [66,69]. Compressive stress is also likely to be due to the native defects arising from the lattice misfit. Native imperfections probably migrate parallel to the film substrate with their surface mobility modified by the substrate temperatures. The origin of the strain is also related to the lattice misfit which in turn depends upon the deposition conditions.

The microstrain (ϵ) developed in the sprayed MnO:B films were calculated from Equation [70],

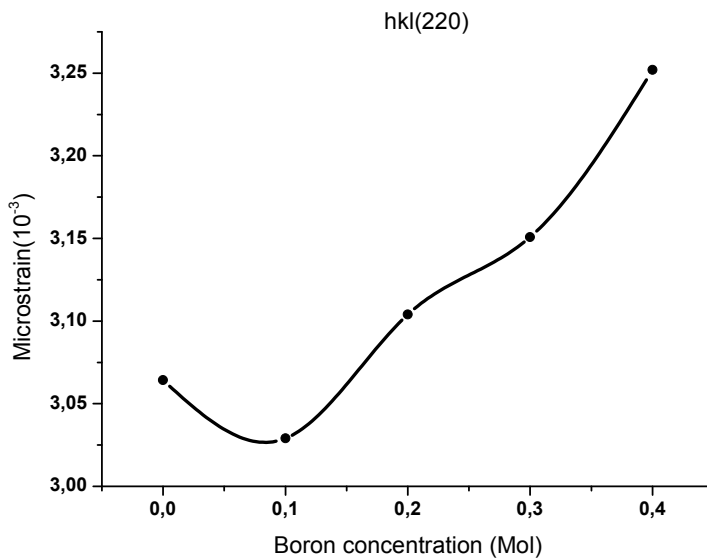
$$\epsilon = D \cos \theta / 4 \quad (4.3)$$

where D is the full width at half maximum of the (111), (220) and (311) peaks and given in Table 4.1. Figure 4.3 shows that the variation of the microstrain (ϵ) with boron concentration in MnO:B films. It is observed from Figure 4.3 that the microstrain (ϵ) decreases with increasing the boric acid concentration up to 0.1 M. This type of change in microstrain may be due to the predominant recrystallization process in the polycrystalline films and due to the movement of interstitial Mn atoms from inside the crystallites to its grain boundary which dissipate and lead to a reduction in the concentration of lattice imperfections [71,72]. Also, from Table 4.1, it is observed that the microstrain decrease with increasing the grain size of the films. This can be attributed to the improvement in crystallinity due to the regular arrangements of atoms in the crystal lattice. This is due to the crystallinity of the films being improved which can be correlated with the increase in the grain size and the XRD results. Moreover one can also notice that the microstrain decreases with

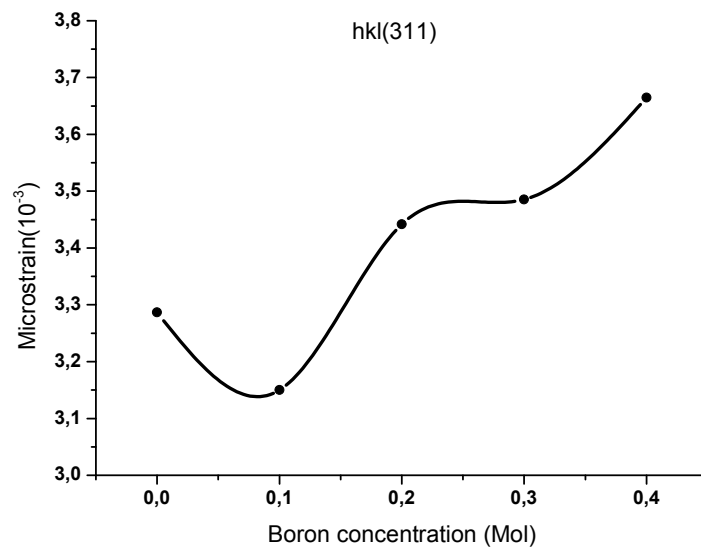
the increase of boric acid concentration up to 0.1 M and then increases with the increase of boric acid concentration. It is clear from the Figure 4.3 and Table 4.1 that there occurs a decrease in internal microstrain within the film and an increase in the crystallite size.



(a)



(b)



(c)

Figure 4.3. Variation of the microstrain (ϵ) with boron concentration in MnO films.

Table 4.1. XRD pattern results of the undoped and boron doped MnO films

SAMPLES	2 θ (Degrees)	Miller Indeces (hkl)	Lattice Constants (a) (Å)	Grain Size (x10 ⁻⁹)	Microstrain ϵ (x10 ⁻³)	Dislocation Density ρ (10 ⁹)/cm ³
Undoped MnO	28.4098	(111)	5.385	1.2039	3.2178	6.686
	47.2858	(220)	5.4327	1.2712	3.0642	6.379
	56.0638	(311)	5.4362	1.2374	3.2869	6.123
0.1 M Boron doped MnO	28.41	(111)	5.4371	1.2895	3.199	6.483
	47.3	(220)	5.4321	1.2969	3.029	6.324
	56.13	(311)	5.4303	1.2717	3.150	6.089
0.2 M Boron doped MnO	28.4	(111)	5.4371	1.1842	3.2524	6.686
	48.1	(220)	5.346	1.2487	3.084	6.395
	56.06	(311)	5.4362	1.1188	3.442	6.1889
0.3 M Boron doped MnO	28.52	(111)	5.4179	1.1606	3.2759	6.7083
	48.02	(220)	5.3545	1.2400	3.1508	6.3974
	56.74	(311)	5.3790	1.0742	3.4855	6.2342
0.4 M Boron doped MnO	28.36	(111)	5.4468	1.0810	3.441	6.775
	47.2858	(220)	5.4327	1.1843	3.252	6.4232
	56.06	(311)	5.4361	1.0617	3.6645	6.2889

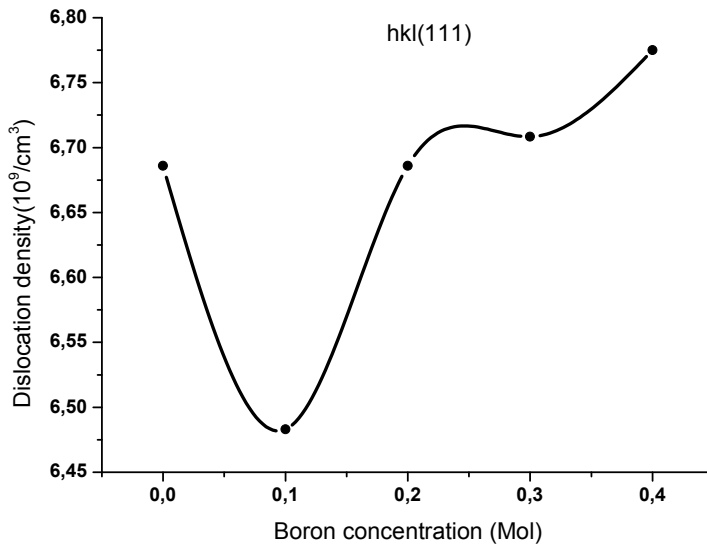
4.6 Dislocation density studies

Dislocations are an imperfection in a crystal associated with the misregistry of the lattice in one part of the crystal with respect another part. Unlike vacancies and interstitial atoms, dislocations are not equilibrium imperfections, i.e. thermodynamic considerations are insufficient to account for their existence in the observed densities. In fact, the growth mechanism involving dislocation is a matter of importance. In this study, the dislocation density is determined from Williamson's and Smallman's method using the following relation for cubic MnO and boron doped MnO films [70] and the variation of the dislocation density with boron concentration is shown in Table 4.1 and Figure 4.4.

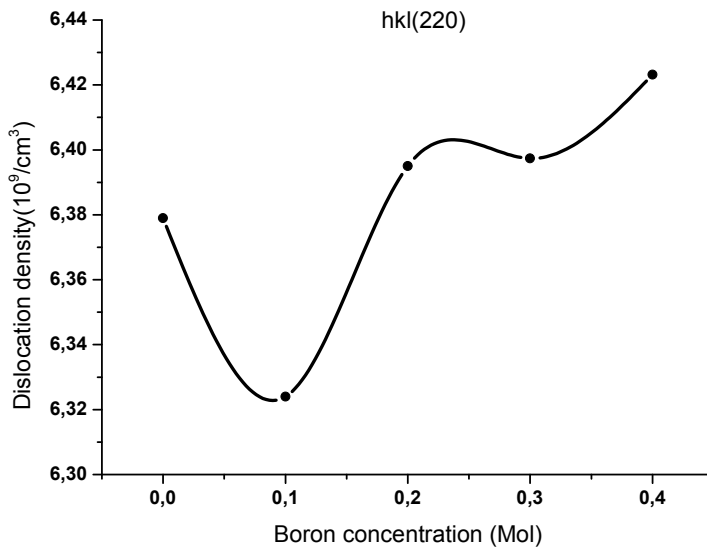
$$\rho = 15\varepsilon/aD \quad (4.4)$$

Figure 4.4 shows the variation of the dislocation density (ρ) with boron concentration in MnO films. The dislocation density (ρ) is defined as the length of dislocation lines per unit of the crystal, and the small ρ means that the crystallization of the films is good. As seen from Table 4.1 and Figure 4.4, dislocation density (ρ) decreases with the increase of boron concentration up to 0.1M and then increases with the increase of boron concentration. It is clear from the Figure 4.4 and Table 4.1 that there occurs a decrease a number of lattice imperfections within the film and an increase in the crystallite size. This may be due to a decrease in the occurrence of grain boundaries because of an increase in the grain size of the film with increase in boric acid concentration up to 0.1M. These parameters indicate the formation of high quality boron doped MnO films deposited on the well cleaned glass substrate by the spray pyrolysis method with dopant contents (up to 0.1M). This can be attributed to the improvement in crystallinity due to the regular arrangements of atoms in the crystal lattice. Therefore, it could be also related to an improvement of the crystallinity leading to a decrease of donor sites trapped at the dislocations and grain boundaries. Also it is observed that the grain size decreases due to the increases the dislocation density and the microstrain at the higher doping level. Since the dislocation density and the microstrain are the manifestation of dislocation network in the films, the increase in the microstrain and the dislocation density indicates the formation of lower quality films at upper boron doping level [73].

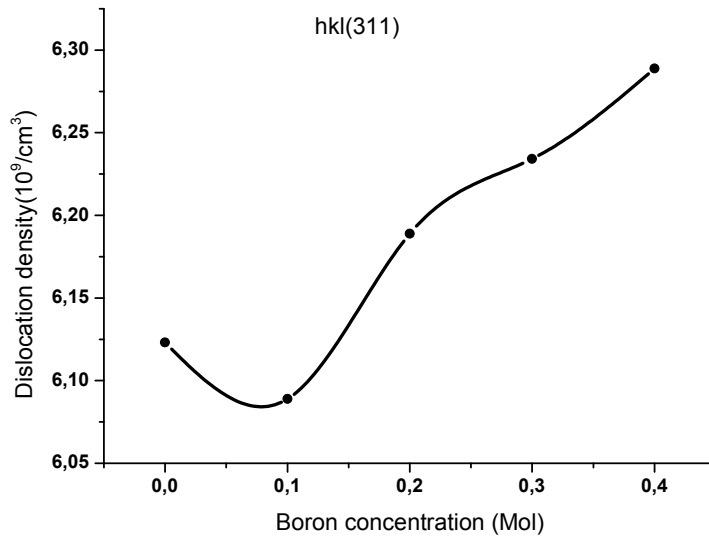
From the above results, we can conclude that boron-doping plays an important role in the crystal orientations of MnO films and effectively modifies the microstructure of the MnO films.



(a)



(b)



(c)

Figure 4.4. Variation of the dislocation density (ρ) with boron concentration in MnO films.

4.7 Optical Studies

Optical absorption studies of the sprayed undoped and boron doped MnO films on the glass substrate have been carried out in the wavelength range of from 300 nm to 900 nm employing a UV/VIS spectrophotometer (Lambda 25 model). The absorption coefficient as a function of photon energy was calculated and plotted for allowed direct transitions (neglecting excitation effects) by using the expression [74,75].

$$\alpha h\nu = A(h\nu - E_g)^{1/2} \quad (4.5)$$

where $h\nu$ is the photon energy, E_g denotes the optical energy bandgap, and A the characteristic parameter (independent of photon energy) for respective transitions.

Figure 4.5 shows that the dependences of $(\alpha h\nu)^2$ as a function of photon energy $h\nu$ indicates the direct nature of band-to-band transitions for the studied samples with the boric acid concentration in solution with (a) 0.1M, (b) 0.2M, (c) 0.3M, (d) undoped and (e) 0.4M. The optical gap (E_g) of the film can be obtained by plotting $(\alpha h\nu)^2$ to $h\nu$ and extrapolating the straight line portion of this plot to the energy axis. The linear dependence of $(\alpha h\nu)^2$ to $h\nu$ indicates that MnO:B films are direct

transition type semiconductors. The photon energy at the point where $(\alpha hv)^2$ is zero is E_g . Table 4.2 gives the optical band gap values obtained by extrapolating the linear portion of the plots of $(\alpha hv)^2$ versus (hv) to $\alpha=0$. These plots are given in Figure 4.5 for the films deposited at 375 °C substrate temperature. It is seen that the slight decreases in the optical band gap of the films with the increasing boron concentration up to 0.1M can be attributed to the increase in the grain size. Another reason could be the improving crystallinity with increasing grain size and this may be due to the extension of electronic states of the impurity phase, precipitates and clusters, into the band gap of MnO:B. This means that the boric acid also affects the band gap of the film. A similar behavior was observed in ZnO:Cu films deposited by spray pyrolysis method [76]. Results of the band gap energy at deposited 450 °C substrate temperature are given in Table 4.1. From Table 4.1, the grain size and band gap energy of the films prepared of 375 °C were approximately changed from 1.3 to 1.0 nm and from 2.25 to 2.54 eV, respectively. As the band gap energy of the film was decreased, the boric acid concentration was increased up to 0.1M, and the grain size of MnO:B films were increased. The change in E_g with boron concentration and grain size was observed in MnO:B films. Therefore, the band gap energy shift of MnO:B films in our study can be attributed to the quantum size effect. The change in E_g with boron concentration of MnO:B films can be understood by the quantum size effect observed in the films of semiconductors.

It is seen at higher doping levels of boron concentration that the band gap was increased, and the grain size of boron doped MnO films were decreased. This broadening in the band gap is known as the Moss_Burstein shift [77]. According to the Moss_Burstein theory, in heavily doped manganese oxide films, the donor electrons occupy states at the bottom of the conduction band. Since the Pauli principle prevents states from being doubly occupied and optical transitions are vertical, the valence electrons require extra energy to be excited to higher energy states in the conduction band. Therefore, the optical band gap (E_{opt}) of doped manganese oxide is broader than that of undoped manganese oxide films. It may be also another reason that defects are accumulated at the grain boundaries. Smaller grain size results in a tensile strain arising from thermal mismatch between the MnO film and the substrate. This indicates that the presence of large number of grain

boundaries increases the defects in the film. The change in E_g with boric acid contents can be correlated with the change of the structural properties of the films.

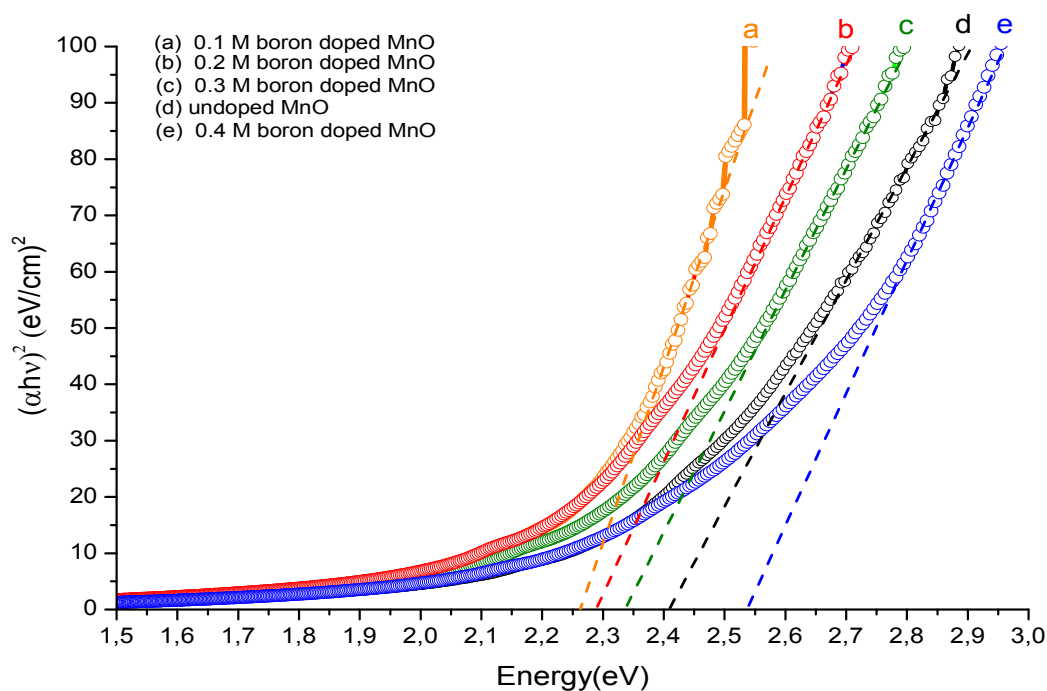


Figure 4.5. A representative graph showing the dependence of $(\alpha hv)^2$ (eV/cm)² on the photon energy hv (eV)

Table 4.2. The band gap values of the samples with respect to the Molar ratio of the manganese chloride and boric acid.

MnO:B films (Molar ratio of the manganese chloride and boric acid)		Band gap of the films E_{op} (eV)
Manganese chloride (1.0M)	Undoped (d)	2.41
Manganese chloride (1.0M)	Boric acid (a) (0.1M)	2.25
Manganese chloride (1.0M)	Boric acid (b) (0.2M)	2.28
Manganese chloride (1.0M)	Boric acid (c) (0.3M)	2.34
Manganese chloride (1.0M)	Boric acid (e) (0.4M)	2.54

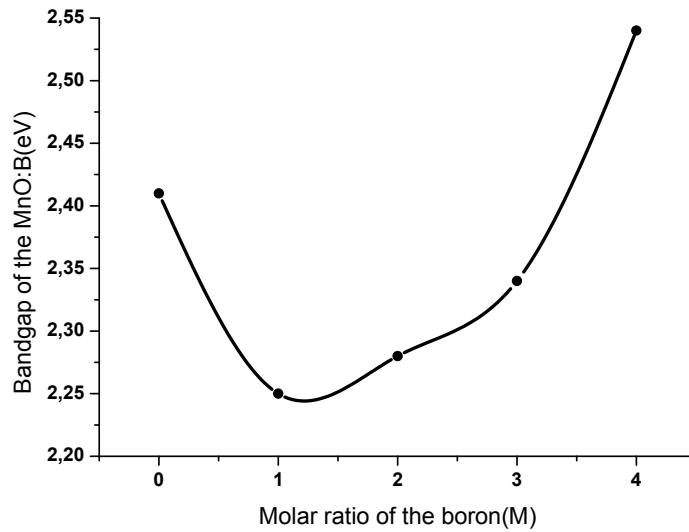


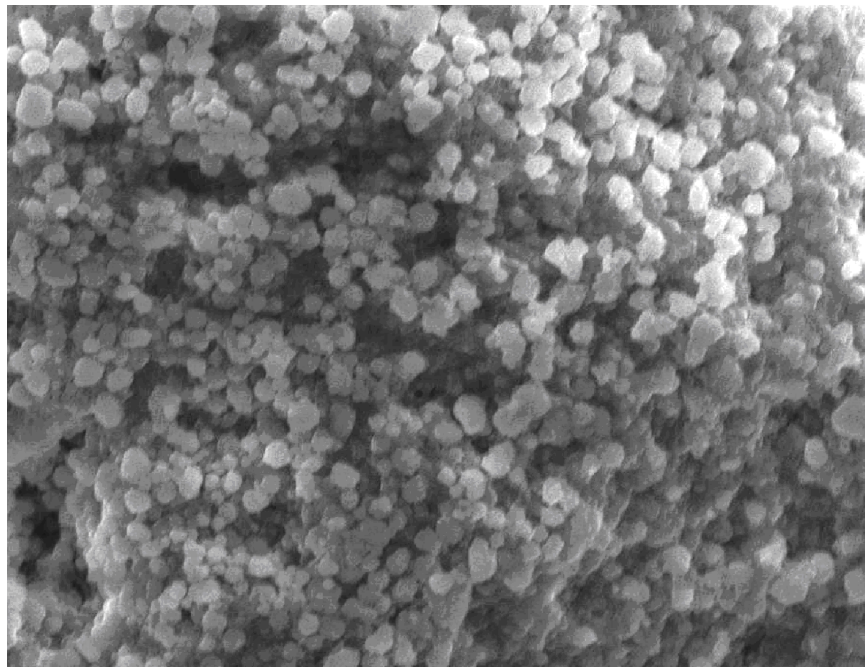
Figure 4.6. Variation of the optical gap E_{opt} with the boron concentration in solution.

Figure 4.6 shows the effect of the boric acid contents on the E_g values for different boron concentration in solution. It can be seen that the band gap first decreases as the boric acid contents increases. This behavior could be attributed to the way that the boron atoms have been incorporated into the film. If Boron is located at substitution sites, then there is an increase in the carrier concentration, and consequently, the band gap narrowing [78,79] shown in Fig. 6 could be due to the Moss–Burstein effect. This effect is taken place for boric acid content $\leq 0.1M$. On the other hand, the trend of increasing E_g for the boric acid content values bigger than $0.1M$, could be attributed to the poor crystallinity of the prepared films or to the formation of the new compound based on B and Mn as has been proposed.

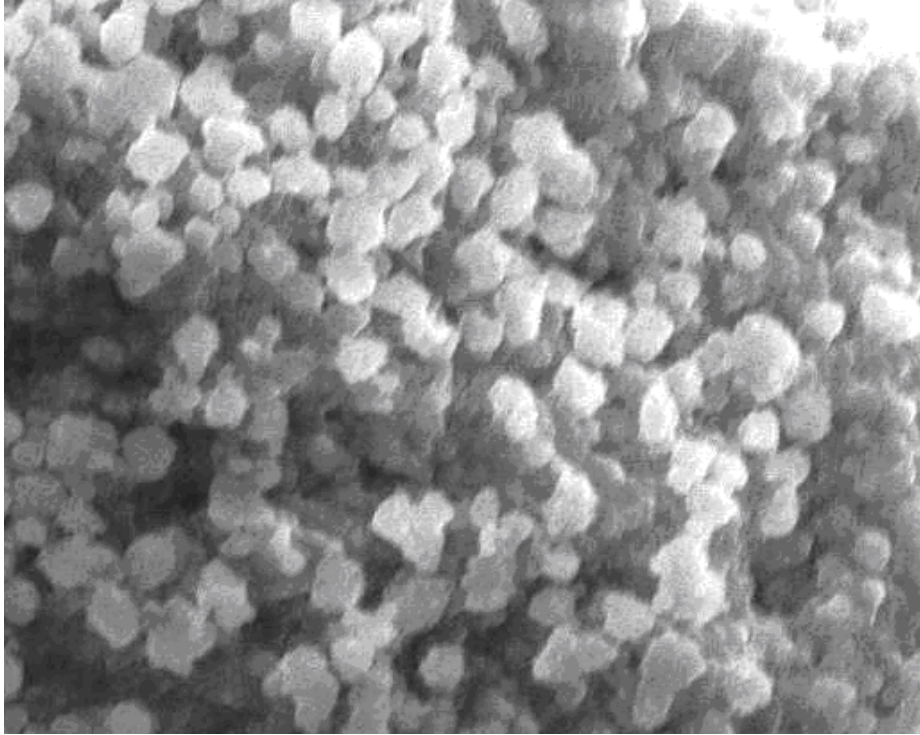
4.8 SEM studies

A scanning electron microscope (SEM) is a type of electron microscope that produces images of a sample by scanning it with a focused beam of electrons. The electrons interact with atoms in the sample, producing various signals that can be detected and that contain information about the sample's surface topography and composition. The electron beam is generally scanned in a raster scan pattern, and the beam's position is combined with the detected signal to produce an image. SEM can achieve resolution better than 1 nanometer. Specimens can be observed in high vacuum, in low vacuum [80].

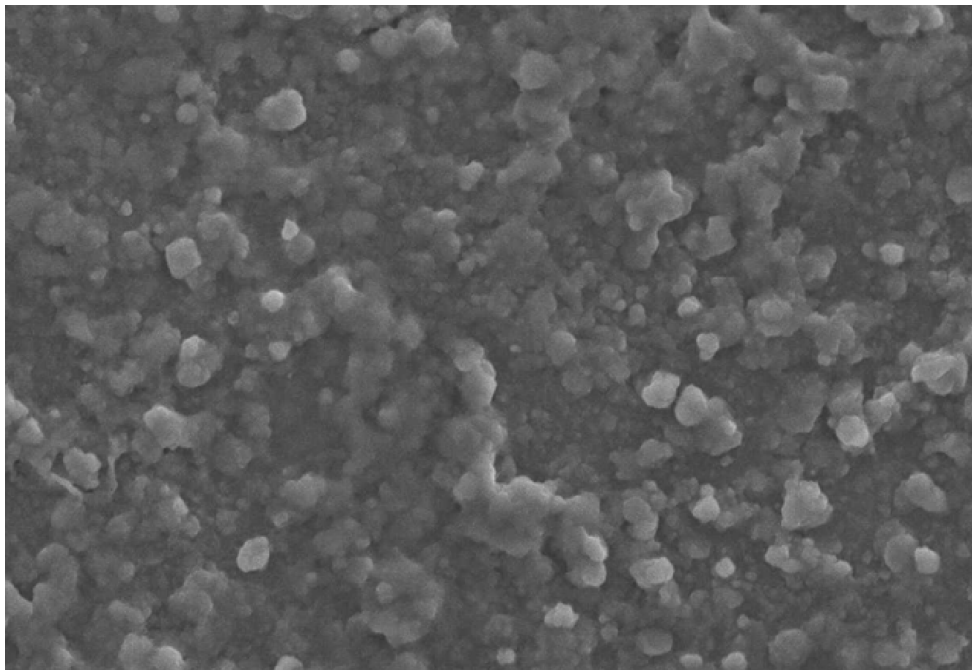
The surface morphology of the sprayed undoped and boron doped MnO films were analysed by scanning electron microscopy (SEM). SEM images of the films are shown in Figure 4.7. SEM image gives valuable information regarding the shape and size of the grains on the surface of the deposited films. In all the cases, the SEM images of undoped and boron doped MnO films reveals rectangular shape grains, which are aggregated. The observed change in the morphology indicates that the boron atoms act as nucleation centers in the vacancy sites of MnO films. The result of the analysis indicates that the boron atoms can influence the grain size. It may be also that the roughness of MnO:B films directly decrease with increasing the boric acid content up to 0.1 M boric acid concentration. Such decreased roughness could be explained as a consequence of an improvement in the grain size with a uniform and more compact surface morphology as evidenced from the SEM images. The SEM images show that the surface morphology of the films is strongly dependent on the concentration of boric acid. This observation correlates with the change in the grain size.



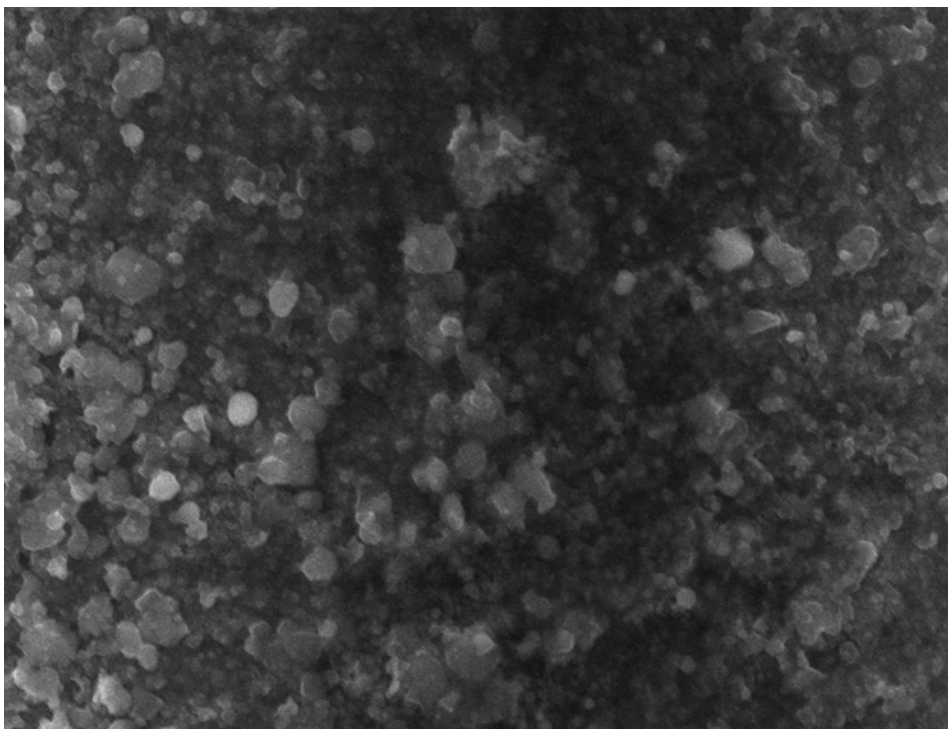
a) Undoped MnO film



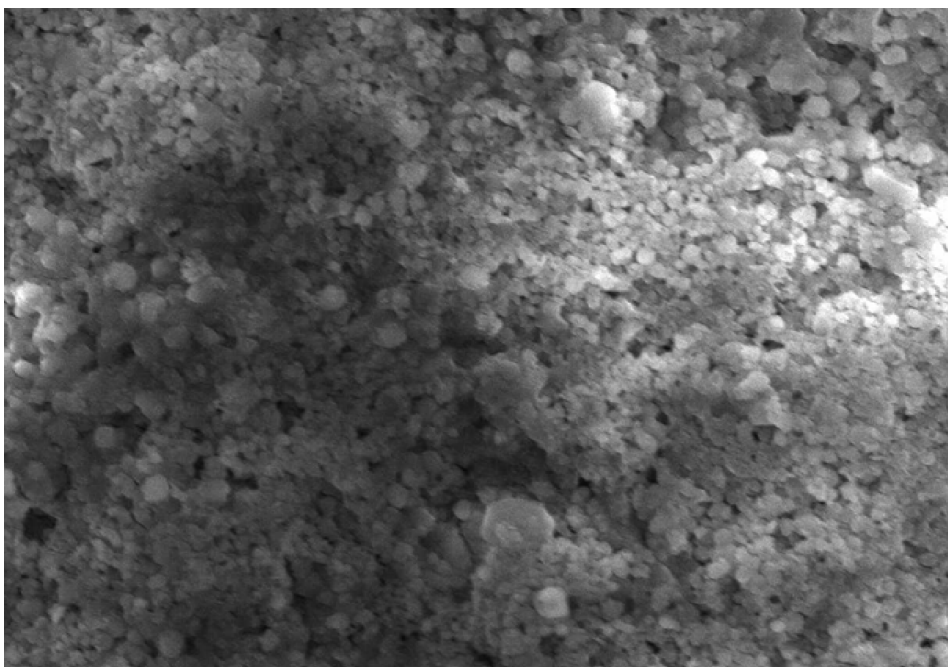
b) 0.1M boron doped MnO film



c) 0.2M boron doped MnO film



d) 0.3M boron doped MnO film



e) 0.4M boron doped MnO film

Figure 4.7. SEM images of the MnO and boron doped MnO films.

4.9 Elemental Analysis

Energy Dispersive X-Ray Analysis (EDX), referred to as EDS or EDAX, is an x-ray technique used to identify the elemental composition of materials or chemical characterization of a sample. It relies on an interaction of some source of X-ray excitation and a sample. Its characterization capabilities are due in large part to the fundamental principle that each element has a unique atomic structure allowing unique set of peaks on its X-ray emission spectrum [81].

The elemental analyses of all films were made by energy dispersive X-ray spectroscopy. The EDS spectra of the MnO films deposited at 375 °C are shown in Figure 4.8. The EDS spectra reveal that the films deposited using perfume atomizer contain the Mn and O which are elements in the starting solution present in the solid films as expected. The quantitative elemental analysis performed through the EDS studies showed that the O/Mn ratios in the film deposited by the simplified and conventional spray techniques was 0.57. It is observed that the MnO film is Oxygen-poor with O/Mn ratio in the deposited film is lower than unity even when the O/Mn ratio in the starting solution is 100. The variation of Mn and O compositions in MnO film with substrate temperature is shown in Table 4.3.

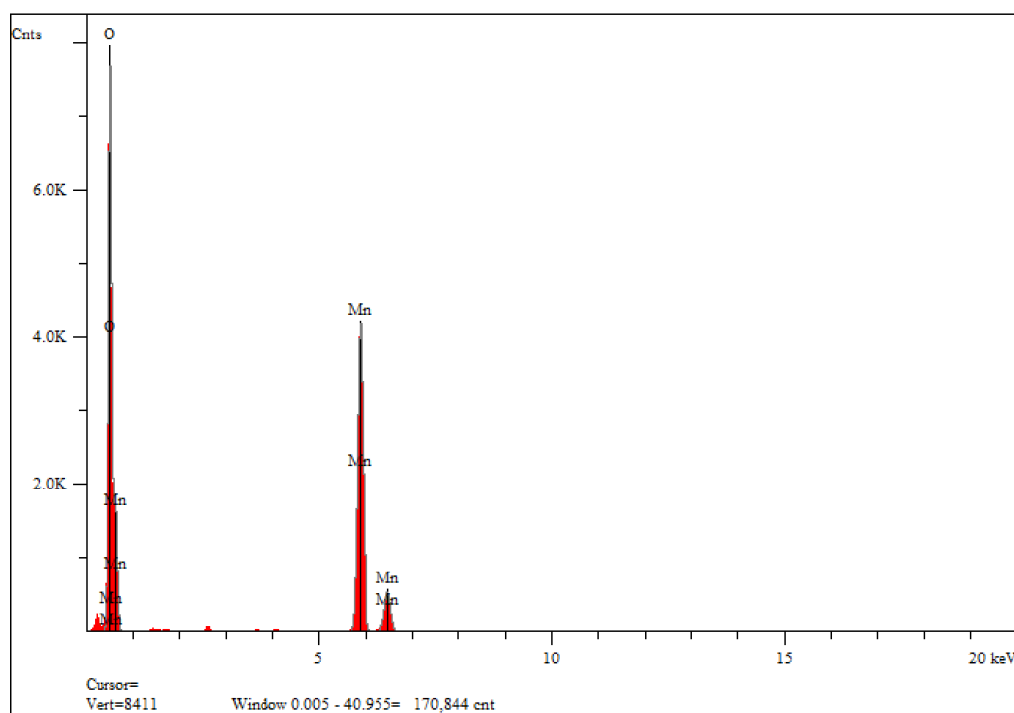


Figure 4.8. EDS spectra of sprayed MnO film.

Table 4.3: The variation of Mn and O compositions in MnO film

Elt.	Line	Intensity (c/s)	Conc	Units	Error 2-sig	MDL 3-sig	
O	Ka	719.66	36.662	wt.%	0.383	0.057	
Mn	Ka	632.81	63.338	wt.%	0.384	0.109	
			100.000	wt.%			Total

5. Conclusion

The X-ray reflection peaks at different planes indicate that films are polycrystalline over the whole range of boron doping concentration studied. The intensity of peaks and crystal orientations are influenced by the boron doping concentration.

It is also observed that the addition of boric acid contents increases the full width at half maximum (FWHM) due to the destruction of the crystal structure and reduction in the grain size.

The lattice constant 'a' first decreases, reaches a minimum value around undoped MnO film and then appears to slowly increase with increasing of the boron doped around the 5.3 and 5.4Å⁰.

The variation of the molar ratio of the boron in the MnO associated with the changes in grain size and boundary.

The crystallinity of the films increase with increase in grain size, which indicates a lower number of lattice imperfections. Due to a decrease in the occurrence of grain boundaries because of an increase on the grain size of the film with increase of boron concentration up to 0.1M concentration of boric acid. These parameters indicate the formation of high quality B-MnO films deposited on the well cleaned glass substrate by spraying pyrolysis method with dopant contents (up to 0.1M).

Dislocation density (ρ) decreases with the increase of boron concentration up to 0.1M and then increases with the increase of boron concentration.

The slight decreases in the optical band gap of the films with the increasing boron concentration up to 0.1M can be attributed to the increase in the grain size.

REFERENCES

- [1] Poortmans, J. Arkhipov, V. (2006). *Thin Film Solar Cells Fabrication, Characterization and Applications*. John Wiley & Sons. ISBN-10: 0-470-09126-6
- [2] Ortega-Lopez M and Morales-Acevedo A (1998). Characterization of CuInS₂ thin films for solar cells prepared by spray pyrolysis. *Thin Solid Films* **330** 96
- [3] Peza-Tapiaa J M, Sanchez-Resendiz V M, Alb or-Aguileraa M, Cayente-Romero J J, De Leon-Gutierrez L R and Ortega-Lopez M (2005). Electrical and optical characterization of Na: CuInS₂ thin films grown by spray pyrolysis. *Thin Solid Films* **490** 142–5
- [4] Badera N, Godbole B, Srivastava S B, Vishwakarma P N, Sharath, Chandra L S, Deepti J, Sathe V G and Ganesan V (2008). Photoconductivity in Cd_{1-x}Mn_xS thin films prepared by spray pyrolysis technique. *Sol. Energy Mater. Sol. Cells* **92** 1646–51
- [5] S.A. Mayen-Hernandez, S.J. Sandoval, R.C. Perez, G.T. Delgado, B.S. Chao, O.J. Sandoval, (2003). *J. Cryst. Growth* **256** 12.
- [6] J. Mu, Z.F. Gu, L. Wang, Z.Q. Zhang, H. Sun, S.Z. Kang, (2008). Phase and shape controlling of MnS nano-crystals in the solvo-thermal process. *J. Nanopartic. Res.* **10** 197–201.
- [7] Z. Pingtang, Z. Qiumei, H. Xianliang, T. Hao, H. Kaixun, (2008). Preparation of γ -MnS hollow spheres consisting of cones by a hydrothermal method. *J. Cryst. Growth* **310** 4268–4272.
- [8] L. David, C. Bradford, X. Tang, T.C.M. Graham, K.A. Prior, B.C. Cavenett, (2003). Growth of zinc blende MnS and MnS hetero-structures by MBE using ZnS as a sulfur source *J. Cryst. Growth* **251** 591.

- [9] E. Jahne, O. Goede, V. Weinhold,(1988). Far Infrared Reflectivity of Tetrahedrally and Octahedrally Coordinated MnS *Phys. Stat. Sol. B* **146(2)** K157-160.
- [10] H.M. Pathan, S.S. Kale, C.D. Lokhande, S.H. Han, O.S. Joo, (2007). Preparation and characterization of amorphous manganese sulfide thin films by SILAR method. *Mater. Res. Bull.* **42** 1565–1569.
- [11] D. Fan, H. Wang, Y.C. Zhang, J. Cheng, B. Wang, H. Yan,(2003). *Mater. Chem. Phys.* **80** 44.
- [12] D.B. Fan, X. Yang, H.Wang, Y. Zhang, H. Yan,(2003). Photoluminescence of MnS thin film prepared by chemical bath deposition. *Physica. B* **337** 165.
- [13] A. Yılmaz, (2011). Characterization of MnS films deposited by the spray pyrolysis method. *Phys. Scr.* **83** 045603 (5pp)
- [14] J. C. Z. Nardi, (1985). Characterization of the Li / MnO₂ multistep discharge *J. Electrochem. Soc.* **132**, 1787.
- [15] L. Sanchez, J. Faray, J.P.Pereira –Ramos, L. Hernan, J. Morales, L. Tirado,(1996). Low-temperature mixed spinel oxides as lithium insertion compounds. *J. Mater. Chem.* **6**, 37.
- [16] R. N. Reddy, R.G. Reddy,(2004). Synthesis and electrochemical characterization of amorphous MnO₂ electrochemical capacitor electrode. *J. Power Sourc.* **132**, 315.
- [17] R. N. Reddy, R. G. Reddy, (2002). Electrochemical capacitor and hybrid powder sources, in: Brodd RJ, et al., *The electrochemical society proceeding series*, PV 2002-7 Pennington NJ, 197.
- [18] C-N Xu, K. Miyazaki, T. Watanable (1998).Humidity sensors using manganese oxides. *Sensors and Actuators B* **46**, 87.
- [19] K. J. Kim, Y. R. Park.(2004). *J. Cryst. Growth* **270**, 162.

- [20] C. N. R. Rao, A. K. Cheetham, (1997). Giant magnetoresistance, charge-ordering, and related aspects of manganates and other oxide systems. *Adv. Mater.* **9**, 1009.
- [21] R. Von Helmolt, J. Wecker, B. Holzapfel, L. Schultz, K. Samwer, (1993). Giant negative magnetoresistance in perovskitelike $\text{La}_{2/3}\text{Ba}_{1/3}\text{MnO}_x$ ferromagnetic films. *Phys. Rev. Lett.* **71**, 2331.
- [22] M. Regulski, R. Prezenioslo, I. Sosnowska, D. Hohlewein, R. S. Schneider, (2004). Neutron diffraction study of the magnetic structure of $\alpha\text{-Mn}_2\text{O}_3$. *J. Alloy. Comp.* **362**, 236.
- [23] A. A. Dakhel (2006). Correlated structural and electrical properties of thin manganese oxide films. *Thin Solid films* **496**, 353.
- [24] G-O. Yu, I. E. Graboy, V. A. Amelichev, A. A. Bosak, A. R. Kaul, B. Giittler, V. L. Sretchnikov, H. W. Zandbergen (2002). *Solid State Comm.* **124**, 15.
- [25] S. Thirumalairajan, K. Girija, M. Sudha, P. Maadeswaran, J. Chandrasekaran, (2008). *Optoelectronics and Advance Materials, Rapid Communications*, **2-12**, p. 779 - 781
- [26] Shull, Strauser, Wollan, (1951). Neutron Diffraction by Paramagnetic and Antiferromagnetic Substances *Phys. Rev.* **83** 333.
- [27] D. Bloch et al., (1975). Stress-induced tricritical phase transition in manganese oxide. *Phys. Rev. Lett.* **35-14** 963–967.
- [28] A. F. Wells, Structural Inorganic Chemistry, 5th ed., (Oxford University Press, Oxford, UK, 1984).
- [29] Sherman D.M. (1984). The electronic structures of manganese oxide minerals. *American Mineralogis.* **69**, 788-799

- [30] Lun S. W. (2003) Structural and electrical properties of MnO films grown by pulsed laser deposition. The Hong Kong Polytechnic University
- [31] Y. Hagiwara, T. Nakada, A. Kunioka (2001). Improved Jsc in CIGS thin film solar cells using a transparent conducting ZnO:B window layer. *Sol. Energy Mater. Sol. Cells* **67**, 267.
- [32] J. Hupkes, B. Rech, S. Calnan, O. Kluth, U. Zastrow, H. Siekmann, M. Wuttig (2006). Material study on reactively sputtered zinc oxide for thin film silicon solar cells. *Thin Solid Films* **502**, 286.
- [33] B.N. Pawar, S.R. Jadkar, M.G. Takwale (2005). Deposition and Characterization of transparent and conductive sprayed ZnO:B thin films. *J. Phys. Chem. Solids* **66**, 1779.
- [34] J. Lee (2004). Raman scattering and photoluminescence analysis of B-doped CdS thin films. *Thin Solid Films* **170**, 451–452.
- [35] K. T. R. Reddy and R. B. V. Chalapathy (1998). Photoacoustic spectroscopy of sprayed CuGa_xIn_{1-x}Se₂ thin films. *Sol. Energy Mater. Sol. Cells* **50**, 19.
- [36] Ilıcan S., Çağlar Y., Çağlar M. (2005). Spray pyrolysis yöntemi ile elde edilen CdZnS filmlerin yapısal özelliklerine hazırlama parametrelerinin etkisi. *Çukurova Üniversitesi Fen Bilimleri Dergisi*, **26-2**
- [37] Arie A. A., Lee J.K. (2011). Effect of boron doped fullerence C60 film coating on the electrochemical characteristics of silicon thin film anodes for lithium secondary batteries. *Synthetic Metals*. **161**, 158-165
- [38] J. Xu, M.C. Granger, Q. Chen, J.W. Strojek, T.E. Lister, G.M. Swain, (1997). Boron-doped diamond thin-film electrode. *Anal. Chem. News Features* **69**, 591A–597A.
- [39] Boonsong K., Chuanuwatanakul S., Wangfuengkanagul N., Chailapakul O. (2005). Electroanalysis of lincomycin using boron-doped diamond thin film electrode applied to flow injection system. *Sensors and Actuators B*. **108**, 627-632

- [40] N. Vinokur, B. Miller, Y. Avygal, R. Kalish, (1996). Electrochemical behavior of boron-doped diamond electrodes. *J. Electrochem. Soc.* **143** L238–L240.
- [41] J. Xu, Q. Chen, G.M. Swain, (1998). Anthraquinonedisulfonate electrochemistry: A comparison of glassy carbon, hydrogenated glassy carbon, highly oriented pyrolytic graphite, and diamond electrodes. *Anal. Chem.* **70**, 3146–3154.
- [42] Yu X.Q., He Y., Sun J.P., Tang K., Li H., Chen L.Q., Huang X.J. (2009). Nanocrystalline MnO thin film anode for lithium ion batteries with low overpotential. *Electrochemistry Communications.* **11**, 791-794
- [43] Kooijman H. (2005) Interpretation of crystal structure determinations. (2014) at: <http://www.cryst.chem.uu.nl/huub/notesweb.pdf>
- [44] Rana F.(2009) ECE 407 Lecture notes. Cornell University. (2014) at: <https://courses.cit.cornell.edu/ece407/Lectures/handout4.pdf>
- [45] Bax J.The Hexagonal Crystal System. (2014) at: http://metafysica.nl/hexagonal_1.html
- [46] Albert G. Guy. 1972. Introduction to Material Science. McGraw-Hill Inc., US. ISBN-10: 0070253102
- [47] Mittemeijer E.J. & Welzel U. (2008) The "state of art" of the diffraction analysis of crystallite size and lattice strain. *Zeitschrift für Kristallographie.* **223**, 552-560
- [48] Electrical resistivity and conductivity. (2014) at: http://en.wikipedia.org/wiki/Electrical_resistivity_and_conductivity
- [49] Semiconductors/What is a semiconductor. (2014) at: http://en.wikibooks.org/wiki/Semiconductors/What_is_a_Semiconductor
- [50] Lukasiak L.& Jakubowski A. (2010) History of Semiconductors. *Journal of Telecommunications and Information Technology.* **1/2010**, 3-9

[51] Cheah, K.W. History of Integrated Circuit. (2014) at:
http://resources.edb.gov.hk/physics/articleIE/ic/ic_e.htm

[52] Leach, W.M. ECE3040 Lecture notes. Chapter 1: Conduction in semiconductors. (2014) at:
<http://users.ece.gatech.edu/mleach/ece3040/notes/chap01.pdf>

[53] Extrinsic semiconductor (2014) at:
http://en.wikipedia.org/wiki/Extrinsic_semiconductor

[54] Sarı, H. Lecture notes (2008). Yarı iletken fiziği:Elektronik ve Optik özellikler. (2014) at: <http://80.251.40.59/eng.ankara.edu.tr/hsari/bolum-11-yariiletkenler-1.pdf>

[55] Direct and indirect band gaps. (2014) at:
https://en.wikipedia.org/wiki/Direct_and_indirect_band_gaps

[56] Garrett P. (2006) PHY-1070 Lecture notes. Absorption and transmission of light and Beer-lambert law. (2014) at:
<http://www.physics.uoguelph.ca/~pgarrett/teaching/PHY-1070/lecture-21.pdf>

[57]Zhang Y. & Shakouri A. (2002) Lab 8: Optical Absorption at:
<http://classes.soe.ucsc.edu/ee145/Spring02/EE145Lab8.pdf>

[58]Bragg' law. (2014) at: http://en.wikipedia.org/wiki/Bragg's_law

[59] Schweitzer J. Scanning electron microscope. (2014) at:
<http://www.purdue.edu/epps/rem/rs/sem.htm>

[60] Cullity, B. D. 1978. Elements of X-ray diffraction. 2nd ed. Addison-Wesley, Reading, Mass. B) Klug, H. P., and L. E. Alexander. 1974. X-ray diffraction procedures for polycrystalline and amorphous materials. 2nd ed. Wiley, New York.

[61] S. Thirumalairajan, K. Girija, M. Sudha, P. Maadeswaran, J. Chandrasekaran (2008) *Optoelectronics and Advance Materials, Rapid Communications*, **2-12**, 779 – 781

- [62] M. Bedir, M.Öztaş, Ö.F. Bakkaloğlu, and R. Ormancı (2005). Investigations on structural, optical and electrical parameters of spray deposited ZnSe thin films with different substrate temperature, *Eur. Phys. J. B* **45**, 465–471
- [63] B.D. Cullity, *Elements of X-Ray Diffraction* (A.W. Pub.Comp. Inc., 1978), pp. 99–106
- [64] H. Kim, J.S. Horwitz, G. Kushto, A. Pique, Z.H. Kafa_, C.M. Gilmore, D.B. Chrisey (2000). Electrical, optical, and structural properties of indium–tin–oxide thin films for organic light-emitting devices. *J. Appl. Phys.* **88**, 6021.
- [65] M. Bedir, M. Öztaş, S.S. Çelik and T. Özdemir (2014). Effect of boric acid content on the structural and optical properties of MnS films prepared by spray pyrolysis technique. *Acta Physica Polonica A*, **126**
- [66] I.A. Ovid'ko (2000). Interfaces and misfit defects in nanostructured and polycrystalline films. *Rev. Adv. Mater. Sci.* **1**, 61
- [67] W.D. Nix, Mec. Proper., Thin Films, Nadai Medal Lecture, ASME Congress, New York, 2001
- [68] S. Lalitha et al. (2000). Characterization of CdTe thin film dependence of structural and optical properties on temperature and thickness. *Solar Energy Materials and Solar Cells* **82**, 187.
- [69] I.M. Khan, in: *Handbook of Thin Film Technology*, Edited by L.I. Maissel, R. Glang (Mc-Graw Hill, New York, 1970), Chap. 10
- [70] C.K. De, N.K. Mishra (1997) *Indian J. Phys. A* **71**, 530.
- [71] F.A. Kroger, *The Chemistry of Imperfect Crystals*, North-Holland, Amsterdam 1964.
- [72] C.F. Rong, G.D. Watkins (1987). Optically detected magnetic-resonance observation of the isolated zinc interstitial in irradiated ZnSe. *Phys. Rev. Lett.* **58**, 1486.

- [73] N. Jabena Begum, K. Ravichandran, (2013). Effect of source material on the transparent conducting properties of sprayed ZnO:Al thin films for solar cell applications. *J. Phys. Chem. Solids* **74**, 841.
- [74] O. Heavens, *Optical Properties of Thin Solid Films* (Dover, New York, 1965)
- [75] J.N. Hodgson, *Optical Absorption and Dispersion in Solids* (Chapman and Hall, London, 1970)
- [76] Mustafa Öztas, Metin Bedir (2008). Thickness dependence of structural, electrical and optical properties of sprayed ZnO:Cu films. *Thin Solid Films* **516** 1703–1709
- [77] E. Burstein (1954). Anomalous Optical Absorption Limit in InSb *Phys. Rev.* **93**, 632.
- [78] B.E. Sernelius, K.F. Berggren, Z.C. Jim, I. Hamberg, C.G. Granqvist (1988). Band-gap tailoring of ZnO by means of heavy Al doping. *Phys. Rev. B* **37**, 10244.
- [79] A. K. Jonscher (1967). *Thin Solid Films* **1**, 213.
- [80] Goldstein, G. I. Newbury, D. E. Echlin, P. Joy, D. C. Fiori, C.; Lifshin, E. (1981). *Scanning electron microscopy and x-ray microanalysis*. New York, Plenum Press. ISBN 0-306-40768-X.
- [81] Joseph Goldstein (2003). *Scanning Electron Microscopy and X-Ray Microanalysis*. Springer. ISBN 978-0-306-47292-3.